



**HAL**  
open science

# Thermal models of oceanic crustal accretion: Linking geophysical, geological and petrological observations

J. Maclennan, T. Hulme, S. C. Singh

► **To cite this version:**

J. Maclennan, T. Hulme, S. C. Singh. Thermal models of oceanic crustal accretion: Linking geophysical, geological and petrological observations. *Geochemistry, Geophysics, Geosystems*, 2004, 5, pp. 200-212. 10.1029/2003GC000605 . insu-03600291

**HAL Id: insu-03600291**

**<https://insu.hal.science/insu-03600291>**

Submitted on 7 Mar 2022

**HAL** is a multi-disciplinary open access archive for the deposit and dissemination of scientific research documents, whether they are published or not. The documents may come from teaching and research institutions in France or abroad, or from public or private research centers.

L'archive ouverte pluridisciplinaire **HAL**, est destinée au dépôt et à la diffusion de documents scientifiques de niveau recherche, publiés ou non, émanant des établissements d'enseignement et de recherche français ou étrangers, des laboratoires publics ou privés.

Copyright



## Thermal models of oceanic crustal accretion: Linking geophysical, geological and petrological observations

**J. Maclennan**

*Laboratoire de Géosciences Marines, Institut de Physique du Globe de Paris, 4, Place Jussieu, Paris 75252 Cedex 05, France (maclenna@ipgp.jussieu.fr)*

*Now at School of GeoSciences, The University of Edinburgh, Grant Institute, The King's Buildings, West Mains Road, Edinburgh EH9 3JW*

**T. Hulme and S. C. Singh**

*Laboratoire de Géosciences Marines, Institut de Physique du Globe de Paris, 4, Place Jussieu, Paris 75252 Cedex 05, France (hulme@ipgp.jussieu.fr; singh@ipgp.jussieu.fr)*

[1] Models of oceanic crustal accretion should be able to reproduce both petrological and geological observations from ophiolites and geophysical observations from active spreading ridges. We have developed thermal models of crustal accretion at fast spreading ridges that incorporate petrological variation and allow for a variable vertical distribution of crystallization. Including petrological variation has a major effect on the distribution of melt within the crust and the consequent interpretation of model results in terms of geophysical observables. In particular, the narrow melt lens imaged by seismic reflection surveys can be produced by the presence of large-scale compositional stratification within the crust, such as that observed in the Oman ophiolite. Controlling the vertical distribution of crystallization allows a range of crustal accretion mechanisms to be tested, including the many sills and gabbro glacier models. Both gabbro glacier and many sills models can broadly match the geophysical observations, but the preferred model is a hybrid, where the uppermost 25% or more of the lower crust forms in a gabbro glacier and the lowermost 25% or more of the lower crust forms by crystallization in situ. The success of all models is dependent on the strength and distribution of hydrothermal cooling.

**Components:** 16,193 words, 12 figures, 2 tables.

**Keywords:** Modelling; petrology; geophysics; crust; oceanic.

**Index Terms:** 3035 Marine Geology and Geophysics: Midocean ridge processes; 3210 Mathematical Geophysics: Modeling; 8439 Volcanology: Physics and chemistry of magma bodies.

**Received** 21 July 2003; **Revised** 26 November 2003; **Accepted** 5 December 2003; **Published** 13 February 2004.

Maclennan, J., T. Hulme, and S. C. Singh (2004), Thermal models of oceanic crustal accretion: Linking geophysical, geological and petrological observations, *Geochem. Geophys. Geosyst.*, 5, Q02F25, doi:10.1029/2003GC000605.

---

**Theme:** The Oman Ophiolite and Mid-Ocean Ridge Processes

**Guest Editors:** Peter Kelemen, Chris Macleod, and Susumu Umino

## 1. Introduction

[2] It is broadly accepted that the oceanic crust forms by crystallization of basaltic mantle melts at mid-ocean ridges. However, the details of this oceanic crustal accretion process are not well resolved, and have been the subject of much debate over the last 30 years. One key problem is determining the distribution of crystallization at spreading ridges, specifically constraining the range of depths over which crystallization occurs. A number of approaches have been used to address this problem, including the acquisition of geophysical, geological and petrological observations from both active spreading ridges and ophiolites and the development of thermomechanical models of crustal accretion. However, the observations and results of the models have not yet allowed a consensus to be reached on the accretion process, and a number of different conceptual models have been proposed.

[3] One class of models, referred to herein as gabbro glacier models, was initially proposed partly in response to geological observations from ophiolites [Sleep, 1975; Dewey and Kidd, 1977; Quick and Denlinger, 1993] and was developed further in order to account for geophysical observations from fast spreading ridges such as the East Pacific Rise (EPR) [Henstock et al., 1993; Phipps Morgan and Chen, 1993]. The essential feature of these models is that melt is supplied directly from the mantle to a shallow melt lens (Figure 1a). While some of the melt is fed upward from the lens to produce dykes and lava, most of it crystallizes at the level of the lens. In order to generate the full thickness of the oceanic crust, this dominantly solid residue of crystallization must flow downward from the lens.

[4] Interpretation of geological and petrological observations from the Oman ophiolite, however, has led to the development of a different class of crustal accretion models, which is referred to as the many sills model herein [Boudier et al., 1996; Kelemen et al., 1997b]. In contrast to the gabbro glacier models, the key feature of the many sills models is that crystallization takes place within the lower crust, so that a substantial portion of the lower crust may be produced in situ (Figure 1b). In the

end-member case where crystallization takes place evenly with depth throughout the crust there is no requirement for vertical flow of solidified material.

[5] Although petrological stratification is known to exist within the oceanic crust [Cann, 1974], it has so far been neglected in thermal modeling studies. Nevertheless, the inclusion of petrological variation has a significant effect on the predicted distribution of melt within the crust [Sinton and Detrick, 1992]. Since the geophysical observations are strongly sensitive to variations in melt fraction it is necessary to include compositional variation in thermal models in order to relate the results of these models to the observations. Furthermore, the presence of large-scale petrological variation is one of the observations from ophiolites that have been used to constrain the oceanic crustal accretion process.

[6] In this paper we develop new models of crustal accretion that include the effects of petrological variation and that are flexible enough to allow for various distributions of crystallization. After introducing the geophysical, geological and petrological observations that are critical to the problem, we proceed to the theoretical development of the new models. The flexibility of the modeling framework then allows the results of a range of models (including gabbro glacier models, many sills models and hybrid models) to be tested for compatibility with observations.

## 2. Geophysical Observations From the East Pacific Rise

[7] Geophysical surveys of the fast spreading EPR have provided several observations that can be used to constrain the distribution of melt within the crust and therefore the crustal accretion process. The presence of melt beneath the ridge axis was first revealed by seismic reflection surveys [Herron et al., 1980; Hale et al., 1982; Detrick et al., 1987]. Further surveys of the EPR have commonly found reflections thought to be caused by a magma lens sitting at depths of 1–2 km beneath the seafloor and with an across-axis width of 0.5–2 km [Kent et al., 1993a, 1993b; Hooft et al., 1997; Babcock et al., 1998; Carbotte et al., 2000]. While the lens is often

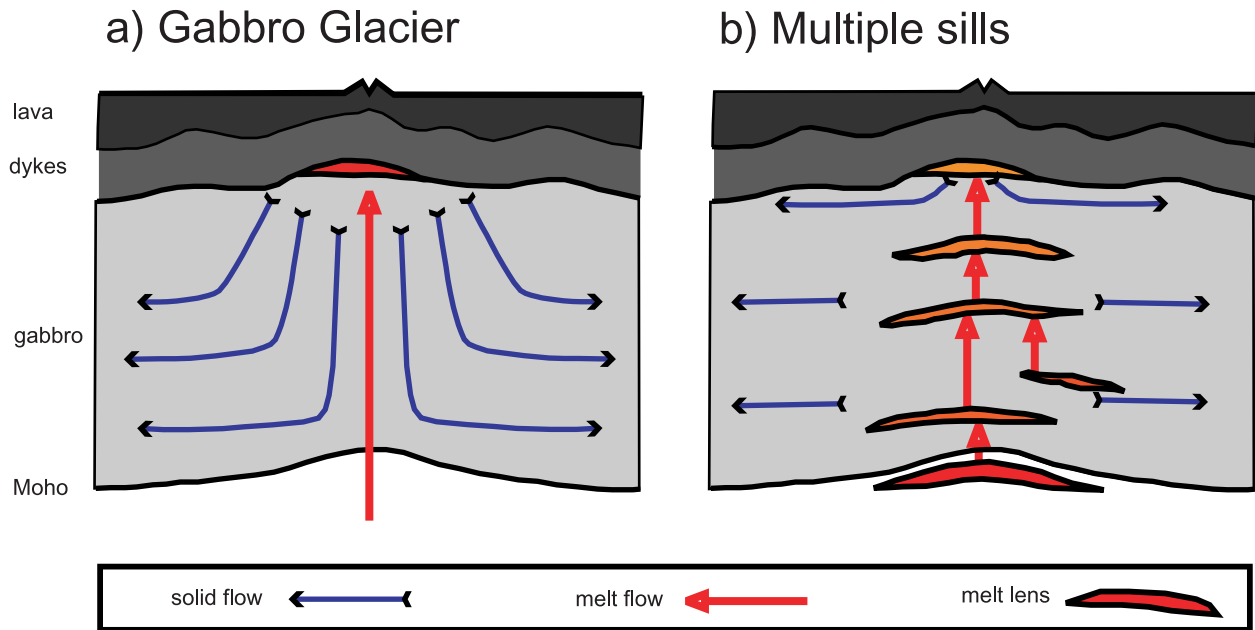


**Figure 1.** Crustal accretion models redrawn from *Korenaga and Kelemen* [1998]. (a) Gabbro glacier model where all crystallization of the lower crust takes place in the shallow melt lens [e.g., *Quick and Denlinger*, 1993]. (b) Many sills models as proposed by *Kelemen et al.* [1997b].

continuous for tens of kilometres along axis, its depth and width can vary dramatically over shorter lengthscales. Further investigation of the lens properties on the southern EPR has indicated that it is less than 100 m thick and may contain either pure melt or partially crystalline mush [*Collier and Singh*, 1997; *Singh et al.*, 1998, 1999]. The lens was inferred to have a near-solid roof and floor and transition zones from the lens into these boundaries are less than 50 m thick. The discovery of the shallow melt lens, and the lack of reflections associated with deeper melt bodies, led to the development of the gabbro glacier models.

[8] Measurements of the seismic velocity structure of ridges using wide-angle seismic data has also been used in support of the gabbro glacier model. The results of early one-dimensional modeling indicated that the melt lens lay at the top of a crustal low velocity zone [*Harding et al.*, 1989; *Vera et al.*, 1990], and a detailed three-dimensional crustal tomographic model of the 9°30'N region of the EPR recovered a low velocity zone in the lower crust with a full across-axis width of 5–8 km [*Dunn et al.*, 2000]. These authors showed that the low velocity zone can be generated if small

melt fractions (<20%) are present in the axial crust. The limited across-axis extent of this zone has been attributed to cooling of the crust in the flanks of the zone by deep hydrothermal circulation.

[9] The physical properties of the lower crust can also be constrained by the use of seafloor compliance measurements. These measurements are consistent with the presence of a zone of small melt fraction in the lower axial crust with an across-axis width of 10 km or less [*Crawford and Webb*, 2002]. Near 9°30'N these workers additionally found a thin, melt-rich region present near to the base of the crust, perhaps reflecting a second melt lens at the Moho. The presence of a melt body at the Moho has also been inferred from observations of converted seismic waves [*Garmany*, 1989]. These observations are not consistent with gabbro glacier models, as they indicate that melt ponds and may crystallize in locations other than the shallow melt lens.

### 3. Geological Observations From the Oman Ophiolite

[10] Geological observations from the Oman ophiolite have been important in the development

of models of crustal accretion at fast spreading ridges. This ophiolite is believed to have escaped extreme deformation during emplacement, and therefore provides the best means available for determining the large-scale structure of fast spreading ridges [Cann, 1974; Nicolas, 1989; Nicolas and Boudier, 1995]. Strong layered fabrics are present in gabbros in the Oman ophiolite, with layering in the lower part of the lower crust being near parallel to the Moho, while fabrics present in the region beneath the dyke zone are perpendicular to the Moho [Pallister and Hopson, 1981; Boudier et al., 1996]. It was originally proposed that this variation in the attitude of layering was due to crystal accumulation on the margins of a large magma chamber with a flat Moho-parallel base and Moho-perpendicular sides [Cann, 1974; Pallister and Hopson, 1981]. After the presence of such large magma chambers at fast spreading ridges had been discounted using the geophysical observations, the layering was subsequently interpreted as being the result of subsidence of solid material from a shallow melt lens, that is, due to a gabbro glacier [Sleep, 1975; Quick and Denlinger, 1993].

[11] Further investigation of these fabrics has shown that there is more than one origin of layering. Gabbros close to the base of the crust exhibit modal layering on the scale of centimeters to meters, so that the base of each layer is rich in mafic minerals while the top has a greater abundance of plagioclase [Pallister and Hopson, 1981; Browning, 1984]. In contrast, the foliated fabric of gabbros that lie in the upper part of the lower crust is caused by the alignment of elongate plagioclase crystals [MacLeod and Yaouancq, 2000]. The foliation and layering do not appear to be physically continuous [Kelemen et al., 1997b]. The differing origin of the fabric is not consistent with the simplest form of the gabbro glacier models since there is no obvious way of converting the foliated fabrics into modal layering during deformation of solid gabbro [MacLeod and Yaouancq, 2000].

[12] Detailed mapping of the Moho Transition Zone (MTZ) of the Oman ophiolite has revealed the presence of layered gabbroic bodies that are encased within and share igneous contacts with

dunites [Boudier et al., 1996; Kelemen et al., 1997b]. These dunites are compositionally, texturally and physically continuous with mantle dunites and harzburgites found beneath the MTZ [Kelemen et al., 1997b]. The contact relationship between the gabbro and the dunite cannot be produced by continuous deformation of the overlying gabbro pile and indicates that these MTZ gabbros formed in situ near the base of the crust. These observations led Boudier et al. [1996] to propose a hybrid model where the foliated gabbros are formed as part of a gabbro glacier, and the layered and MTZ gabbros are produced in situ near the base of the crust.

#### 4. Petrological Observations

[13] The argument that the MTZ gabbros and lower layered gabbros share a common petrogenesis is consistent with petrological observations. While mineral compositions and modal mineralogy vary within the MTZ and layered gabbros, they both have the compositions of the solid residues of fractional crystallization of basaltic magma. Indeed, Kelemen et al. [1997b] demonstrated that many of the MTZ and lower gabbros have the compositions of solids that are in equilibrium with the basaltic melts that constitute the dyke and lava sections of parts of the ophiolite. The petrological and textural similarities between the MTZ and layered gabbros prompted Kelemen et al. [1997b] to devise the many sills model as it is shown in Figure 1b. Within this model the bulk of the lower crust is produced by fractional crystallization in situ, and the evolved liquids are expelled to higher levels within the crust. While many foliated gabbro samples have mineral compositions that are similar to those found in the layered gabbros, a thin layer of gabbros with the compositions of basaltic melts has been found just beneath the dyke-gabbro transition, implying that melts were not effectively expelled after the onset of crystallization of these gabbros. This layer is only a few tens of meters thick, is compositionally and texturally diverse, and MacLeod and Yaouancq [2000] have suggested that it may correspond to the level of the melt lens imaged at fast spreading ridges. Evidence that such petrological stratification is present in

oceanic crust formed at the EPR comes from observations of compositions of both mid-ocean ridge basalt at the EPR and of gabbroic samples from the Hess Deep [Sinton and Detrick, 1992; Hekinian et al., 1993]. Fine-scale correlation of the mineral chemistry within lower layered gabbros has been used to constrain the flux of melt through intergranular porosity in the gabbros [Korenaga and Kelemen, 1998]. These authors inferred that only a few percent of the total melt flux is transported by porous flow in the gabbros, and reasoned that the limited extent of deformation of observed in the lower gabbros could not have resulted from a gabbro glacier model where small intergranular porosities were present.

## 5. Previous Thermal Models of Oceanic Crustal Accretion

[14] All models of oceanic crustal accretion are similar in that they have to provide a mechanism for the removal of the latent and specific heat released during cooling and crystallization of rising mantle melt [Sleep, 1975]. Conduction, advection and hydrothermal cooling are the principal means of removing this heat, and the different models that are described below implement the cooling in different ways. The models described are all two-dimensional and steady state, having been developed to simulate behavior at fast spreading ridges where along-axis variations in axial morphology and the distribution of melt in the crust are relatively modest.

[15] Some of the earliest images of axial melt lenses at mid-ocean ridges prompted the development of the thermal model of crustal accretion of Morton and Sleep [1985]. These authors modelled the thermal structure of the ridge by balancing the latent and specific heat supplied by magma that is injected at the ridge axis with heat loss by conduction and by hydrothermal activity. While the mass of magma was supplied evenly at the ridge axis, latent heat release was concentrated in the upper half of the crust. By varying the model spreading rate and the strength of the hydrothermal circulation Morton and Sleep [1985] were able to match the depth of the observed melt lenses.

[16] When wide-angle seismic results became available, however, they indicated that the lower crust at the ridge axis is predominantly solid. These observations led to the development of thermomechanical models which were devised to reproduce the shallow melt lens, near-solid lower crust and the attitude of the gabbro layering from Oman [Henstock et al., 1993; Phipps Morgan and Chen, 1993]. Instead of providing an even supply of melt to the ridge axis, the melt is fed directly from the mantle to a shallow melt lens where crystallization of the lower crust takes place. The lower crust is then advected to its final depth in a gabbro glacier. These models included the effect of hydrothermal cooling by allowing for regions of increased conductivity, by up to a factor of 10, in parts of their models. These modelers were able to successfully match the depth of the melt lens reflector and the limited melt fractions within the axial lower crust.

[17] After the initial development of these gabbro glacier thermal models it became clear that the vertical distribution of crystallization that they entailed was at odds with the observations from Oman. In response to these geological observations and the seafloor compliance measurements, Chen [2001] developed an extension of the gabbro glacier model where crystallization was allowed to occur both within the shallow melt lens and within a melt lens at the Moho. The model results indicated that if more than 10% of the lower crust formed by crystallization in the Moho melt lens then a large melt zone would be generated at the base of the crust, having a full across axis width of over 4 km and a thickness of over 1 km. There is no geophysical evidence that a melt zone of this size exists at the base of the crust, leading Chen [2001] to reemphasise the importance of the shallow melt lens in the crustal accretion process.

[18] While the existing thermal models successfully reproduce the broad geophysical observations from active ridges, there remain a number of outstanding problems. The first is that none of these models has been specifically developed to reproduce the thermal structure that would result from the many sills accretion model as proposed by Kelemen et al. [1997b].

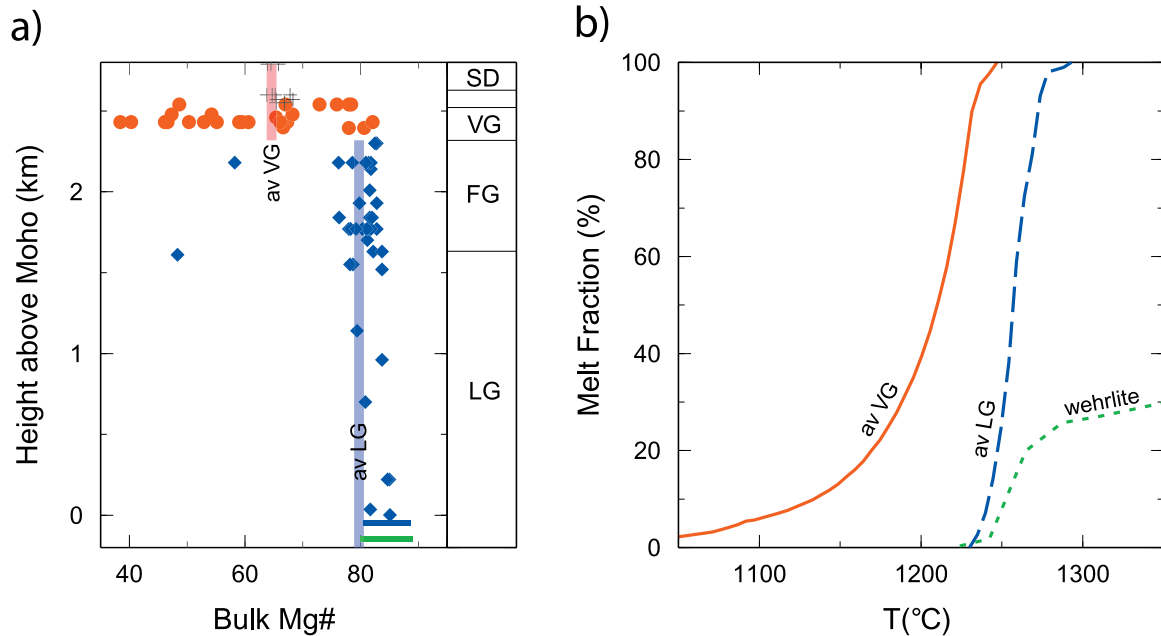


**Figure 2.** (a) Compositional profile of a section through the Oman ophiolite at Wadi Abyad [MacLeod and Yaouancq, 2000]. The height shown is stratigraphic height above the Moho and the composition is expressed as bulk rock Mg#, that is, molar  $\text{Mg}/[\text{Mg} + \text{Fe}^{2+}]$ . Lower crustal gabbros compositions are shown as blue diamonds, gabbros from the varitextured layer just beneath the dykes are red circles and dyke compositions are shown as black crosses. The column to the left shows the lithostratigraphy, through layered gabbros (LG) and foliated gabbros (FG) in the lower crust through to the varitextured gabbros (VG), dyke root zone (unmarked) and sheeted dyke complex (SD). The horizontal bars at the base of the plot show the composition of Moho Transition Zone (MTZ) rocks from the Maqsad Massif [Korenaga and Kelemen, 1997; Koga *et al.*, 2001]. These bars show the compositional range of olivine compositions from gabbros (blue bar) and wehrlites (green bar) in the MTZ and represent minimum estimates of bulk rock Mg#. The vertical pink bar at the top of the plot shows the average varitextured gabbro composition, and the vertical blue bar shows the average lower gabbro composition. (b) Equilibrium melting/crystallization behaviour of average varitextured gabbro (red solid line), lower crustal gabbro (blue dashed line) and wehrlite (green dotted line) from (a). The curves were calculated using the MELTS algorithm with a model pressure of 0.1 GPa and an oxygen fugacity one log unit beneath the fayalite-quartz-magnetite buffer.

[19] A second major problem is that previous thermal models have neglected the effects of petrological variation. There are several reasons why this omission is problematic. Firstly, the presence of petrological variation within ophiolites indicates that large-scale melt-crystal separation took place, and this separation may alter the distribution of latent and specific heat release within the crust. Secondly, observations of petrological variation have played an important role in the development of conceptual models of crustal accretion, so the petrological observations should be used either to constrain or test the thermal modeling. Finally, the incorporation of petrological variation is important because composition controls the relationship between the temperature structure and the predicted geophysical observations [Sinton and Detrick,

1992]. The reason for this control is that the geophysical observations are sensitive to the distribution of melt, and, in order to estimate the melt fraction present in the crust both the local temperature and composition must be known.

[20] The importance of compositional variation in controlling the melting and crystallization behavior of crustal rocks is shown in Figure 2. Thermodynamic modeling indicates that rock having the composition of average lower crustal gabbros in Oman is solid at temperatures of 1210°C and less. In contrast, a rock with the average composition of the gabbros found within ~100 m of the gabbro-dyke transition zone is over 90% molten at this temperature. At 1210°C rocks with these two different compositions will have quite different

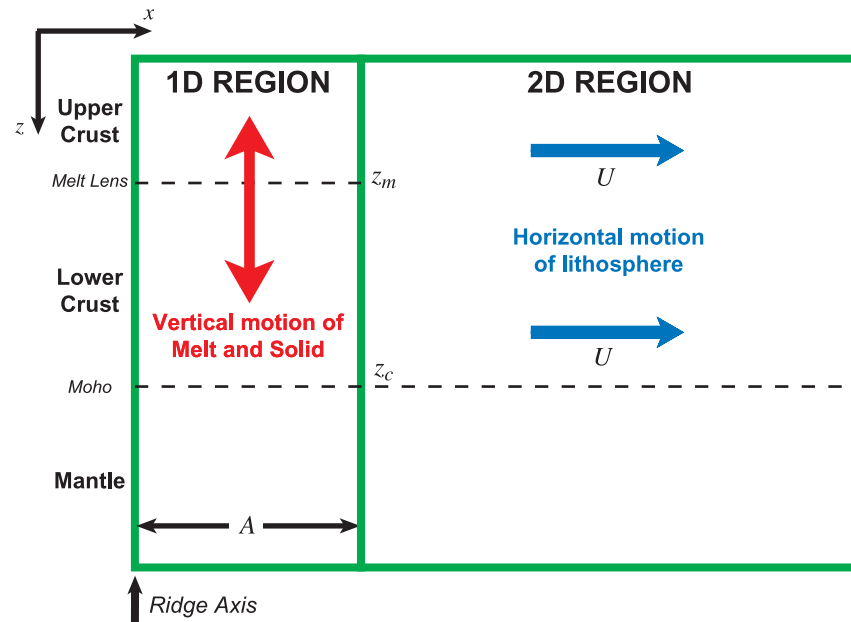


**Figure 3.** Geometry of model. Only one half of the ridge is modelled, and reflected symmetry across the ridge axis, at  $x = 0$ , is assumed. In this case only the right-hand side of the ridge is shown. For definitions of symbols see Tables 1 and 2 and the text.

seismic properties, with the seismic P and S wave velocity of lower crustal gabbro being up to  $3 \text{ km s}^{-1}$  higher than that of the varitextured gabbro [Mainprice, 1997]. Previous thermal models of crustal accretion have neglected the effects of petrological variation, but as these results show, the presence of such variation can enormously affect the geophysical observables interpreted from a thermal structure. Incorporating petrological variation within the modeling process is thus of primary importance in testing model results for compatibility with field observations.

## 6. New Thermal Models of Crustal Accretion

[21] The modeling approach taken in this paper differs from previous studies in three main ways. Firstly, intrusion of melt is modelled as taking place over a range of horizontal positions, rather than just at the ridge axis, in order to reproduce the across-axis width of the axial zone observed by geophysical surveys. Secondly, petrological variation is explicitly taken into account. Thirdly, the models are designed so that the distribution of crystallization with depth can be specified directly and varied in a

straightforward and flexible fashion. This flexibility allows the thermal structures resulting from different distributions of crystallization, such as the gabbro glacier or many sills models, to be determined and compared with the available observations. We restrict attention to two-dimensional steady state models.

### 6.1. Model Geometry

[22] The model geometry, shown in Figure 3, is split into two regions: an axial region and an off-axis region. Intrusion of melt is modelled as taking place uniformly across the axial region, which is of width  $A$  (see Tables 1 and 2 for details of the notation used), and both melt and solid are allowed to flow vertically through this region. Large-scale fractionation of melt and solid can also take place in the axial region, allowing compositional variation to be generated. The temperature structure within the axial region is one-dimensional, varying with depth only, and satisfies an ordinary differential equation derived by balancing mass and heat flowing in and out of the region at each depth. Within the off-axis region, all material is advected horizontally at the half spreading rate of the ridge,  $U$ . The temperature structure is two-dimensional,

**Table 1.** List of Parameters

Symbol	Quantity	Value	Unit	Dimension
$U$	Spreading half-rate	$1.9 \times 10^{-9}$	$\text{m s}^{-1}$	$\text{L T}^{-1}$
$\rho$	Density	$2.9 \times 10^3$	$\text{kg m}^{-3}$	$\text{M L}^{-3}$
$c_p$	Specific heat capacity	$1.085 \times 10^3$	$\text{J kg}^{-1} \text{ }^\circ\text{C}^{-1}$	$\text{L}^2 \text{ T}^{-2} \Theta^{-1}$
$L_h$	Latent heat capacity	$5.06 \times 10^5$	$\text{J kg}^{-1}$	$\text{L}^2 \text{ T}^{-2}$
$k$	Thermal conductivity	2.52	$\text{W m}^{-1} \text{ }^\circ\text{C}^{-1}$	$\text{M L T}^{-3} \Theta^{-1}$
$\kappa \equiv \frac{k}{\rho c_p}$	Thermal diffusivity	$8.0 \times 10^{-7}$	$\text{m}^2 \text{ s}^{-1}$	$\text{L}^2 \text{ T}^{-1}$
$z_c$	Crustal thickness	$6.0 \times 10^3$	m	L
$z_m$	Depth to melt lens	$2.0 \times 10^3$	m	L
$z_l$	Depth of horizontal isotherms	$2.0 \times 10^4$	m	L
$z_g$	Depth to base of mantle melting region	$1.0 \times 10^5$	m	L

satisfying an advection-diffusion equation with source terms due to hydrothermal circulation and latent heat release [Morton and Sleep, 1985]. The depth of the base of the crust is  $z_c$ , and crystallization only occurs within the crust. The depth of the shallow melt lens is fixed at  $z_m$ . In order to simulate the petrological effects of rapid cooling in dykes or lava flows, no separation of melt and solid occurs shallower than  $z_m$ . For models which involve an uneven vertical distribution of crystallization within the crust, such as the gabbro glacier models,  $z_m$  is also the depth where crystallization is focused, and thus acts as the source for the down-flowing solid material of the gabbro glacier. This overall geometry is a gross approximation of the flow field, which in reality is likely to be complex [Chenevez et al., 1998], but the details of the actual flow geometry are poorly known. The simple flow field nevertheless captures the essence of the problem, and allows flexibility in the specified distribution of crystallization.

## 6.2. Input Distributions

[23] Three distributions control the thermal structure, compositional structure and distribution of

melt predicted by the models. These distributions, which are described below, are varied in order to obtain the results shown in section 7.

### 6.2.1. Distribution of Crystallization

[24] The difference between gabbro glacier and many sills models lies in the vertical distribution of crystallization within the axial region. Focussing of crystallization at a given depth within the crust is tied to the flux of melt and and solid and controls the release of latent heat and advection of heat within the axial region. The distribution of crystallization is modelled through the introduction of a function  $\theta(z)$ , defined as the proportion of the lower crust at depth  $z$  that has crystallized in the upper melt lens at  $z_m$ . Defining the flux of fluid through the axial region as  $\mathcal{F}_f(z) \hat{z}$ , and the flux of solid by  $\mathcal{F}_s(z) \hat{z}$  (where  $\hat{z}$  is a unit vector with  $z$  increasing downward), a simple mass balance gives the equations

$$\frac{d\mathcal{F}_s}{dz} = -\theta U, \quad \frac{d\mathcal{F}_f}{dz} = -(1 - \theta)U. \quad (1)$$

The boundary conditions are that  $\mathcal{F}_f(z_c) = -Uz_c$  (enough melt must be supplied at the Moho to form the entire crust) and  $\mathcal{F}_s(z_c) = 0$  (no solid is advected

**Table 2.** List of Variables

Variable	Meaning	Unit	Dimension
$T$	Temperature	$^\circ\text{C}$	$\Theta$
$T_i$	Intrusion temperature	$^\circ\text{C}$	$\Theta$
$A$	Width of axial intrusion region	m	L
$H$	Hydrothermal heat extraction	$\text{W m}^{-3}$	$\text{M L}^{-2} \text{ T}^{-3}$
$\theta$	Fraction of crust made in melt lens	–	1
$\phi$	Fraction of crystallization melt has undergone	–	1
$\gamma$	Crystal fraction of lower crust produced in melt lens	–	1
$\sigma$	Crystal fraction of lower crust produced in sills	–	1
$\tau$	Total crystal fraction of crust	–	1

into the mantle), and so these equations can be solved to give

$$\mathcal{F}_s(z) = U \int_z^{z_c} \theta(\zeta) d\zeta, \quad (2)$$

$$\mathcal{F}_l(z) = -Uz - U \int_z^{z_c} \theta(\zeta) d\zeta, \quad (3)$$

which are then used in the thermal balance described in section 6.3.

### 6.2.2. Style of Crystallization

[25] In order to generate large scale (100s–1000s of meters) compositional stratification within the crust it is necessary to include magmatic differentiation through separation of melt and crystals in the models. This is realized through a function  $\phi(z)$ , which tracks the extent of fractional crystallization that a batch of magma has undergone before it intrudes at depth  $z$ . At the base of the crust  $\phi = 0$ , since no crystallization has taken place. The subsequent evolution of  $\phi(z)$  with depth depends on what is referred to here as the style of crystallization.

[26] Two styles of crystallization are permitted within the models, and these are shown in Figure 4. When melt is frozen rapidly on intrusion, no large scale separation of melt and crystals can take place. Therefore the bulk composition of the solidified material will be the same as that of the original intruded melt. This style of crystallization is called dyke style crystallization (because that is what would be expected to occur in dykes), although it may equally correspond to freezing in lava flows or any rapidly cooled intrusion. A model where all of the crust is made by dyke style crystallization is shown in Figure 5a. Since melt is supplied directly from the mantle to all levels in the crust, and therefore has not undergone any fractional crystallization before it arrives at its final depth,  $\phi = 0$  throughout the crust.

[27] The second permitted style of crystallization is sills style crystallization, where separation of melt and solid is rapid compared to crystallization. During fractional crystallization the compo-

sition of the solid material produced is different to that of the original melt, so the composition of the melt evolves during crystallization. Therefore when melt arrives at a given depth it undergoes an increment of crystallization, deposits the solid products of crystallization and then moves to shallower levels in the crust to continue crystallizing. This separation of liquid and melt allows the models to reproduce the large scale compositional stratification observed in ophiolites, where the lower crustal gabbros are the solid residues of fractional crystallization, and the upper crust has the composition of melt that has risen through the crust. The sills model in Figure 5b has  $\theta = 0$  everywhere, and so  $\phi$  increases uniformly from zero at the Moho to one at the seafloor, reflecting the fact that crystallization proceeds uniformly throughout the crust, and that an increment of mass is lost from the melt by crystallization at each depth before the melt rises to shallower levels.

[28] In the model shown in Figure 5c the crust at depths shallower than  $z_m$  is formed by dyke injection. Below this depth crystallization takes place in sills and there is a single composition generated at each depth. Within the dyking region all material is supplied directly from a depth  $z_m$ , and so  $\phi$  is constant. The value of the constant can be determined by noting that any material that goes into making the upper crust must already have undergone enough crystallization to form the lower crust, and as the lower crust occupies a fraction  $1 - z_m/z_c$  of the total crust,  $\phi = 1 - z_m/z_c$  throughout the dyke section.

[29] In the gabbro glacier model shown in Figure 5d melt is fed directly from the mantle to the shallow melt lens, and therefore arrives at  $z_m$  with  $\phi = 0$ . This melt then has to lose enough mass through crystallization to generate the lower crust and so before melt can be supplied from the melt lens to shallower levels, the fraction crystallized,  $\phi$ , must equal  $1 - z_m/z_c$ . Therefore in models where crystallization is focused in the shallow melt lens, a discontinuity is present in  $\phi$  at  $z_m$ . In general terms, when part of the lower crust crystallizes in situ and the rest is

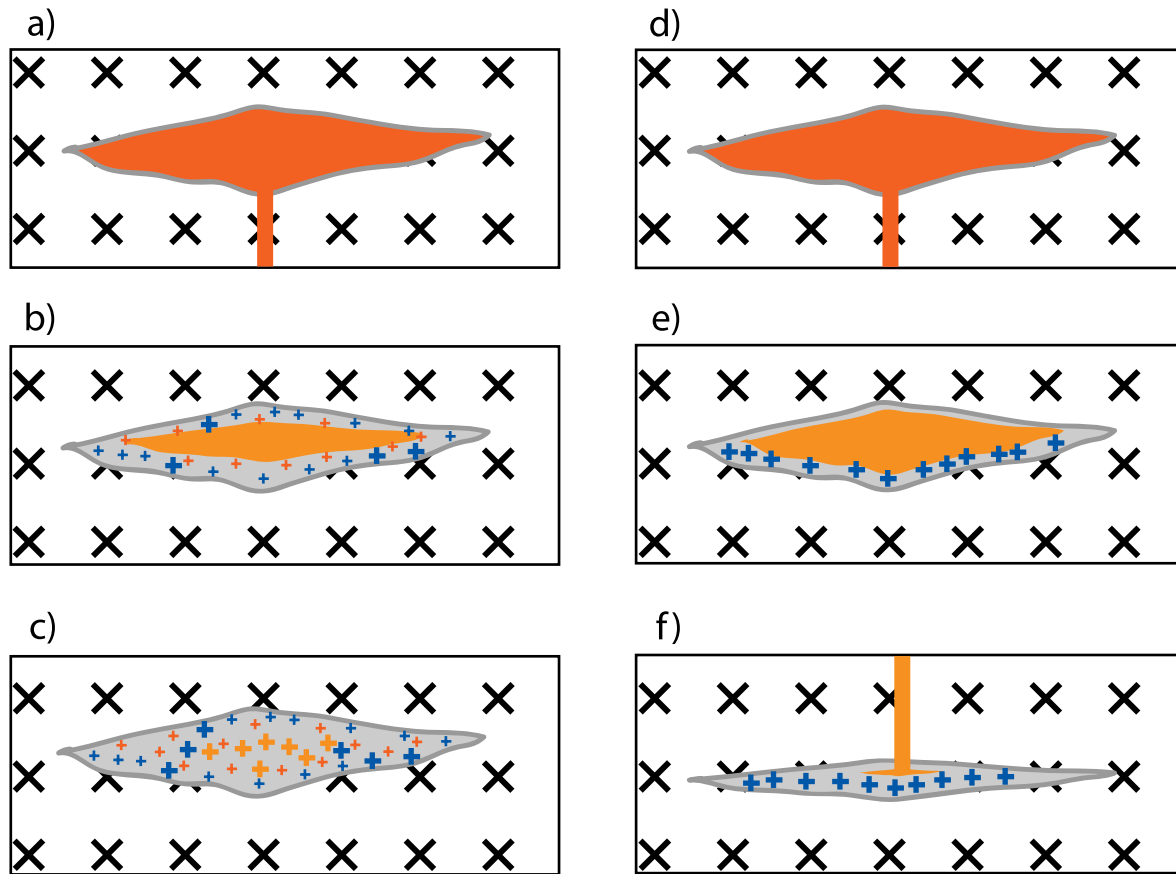


**Figure 4.** Style of crystallization. Parts (a) to (c) show dyke style crystallization, while (d) to (f) show sills style crystallization. The compositions of the melt and solid produced are colour coded, with blue being high Mg# (that of the first cumulates produced), red being intermediate (close to that of mantle melt), and orange being that of evolved melt. Melts are shown as colour fill, while solid is shown as a grey fill with appropriate colour of cross overlaid. (a) Intrusion of primitive magma. (b) Rapid closed-system crystallization occurs without separation of the melt. (c) At solidification, the bulk composition of the solid intrusion is that of the original melt, but on the local scale compositional variation may result from the closed system fractional crystallization. (d) Intrusion of melt. (e) Crystals separate rapidly from the melt, generating a cumulate layer (blue crosses) with a different composition to that of the melt (orange fill). (f) Evolved melt separates from solid and moves to shallower levels in the crust. This leaves a layer of high Mg# cumulates at depth, with little compositional variation.

**Figure 5.** Relationship between distribution of crystallization with depth, compositional structure, melt input temperature and melting behaviour. The first column of plots shows the distribution and style of crystallization for four models. (a) Dyke style crystallization with a uniform distribution of crystallization with depth. (b) Sill style crystallization with a uniform distribution of crystallization. (c) Lower crust formed by sills, upper crust by dykes, with a uniform distribution of crystallization. (d) Lower crust formed in a gabbro glacier and upper crust formed in dykes, with all of the lower crust formed by crystallization at 2 km depth. The grey shading in the first column show regions where no vertical separation of melt and solid takes place after fractional crystallization (dyke style crystallization). The red line shows the value of  $\phi$ , the fraction of the original mantle melt that has been lost through crystallization before the melt reaches a given depth. The blue dotted line is  $\theta$ , the fraction of solid at a given depth that has been generated by crystallization in the shallow melt lens at  $z_m$ . The second column of plots shows the average bulk Mg# of the predicted crustal composition (red line) and the range of Mg# generated by fractional crystallization (grey shaded area). The third column shows the melt input temperature (red line), the crustal solidus and liquidus (blue dotted lines) and the melting range (grey shaded area).

fed downward from the lens, the fraction of total crust produced below  $z_m$  is

$$\phi_0 = \left( z_c - z_m - \int_{z_m}^{z_c} \theta(\zeta) d\zeta \right), \quad (4)$$

while as explained above  $\phi = \phi_1 = 1 - z_m/z_c$  in the dykes. A discontinuity of  $\phi_1 - \phi_0$  is therefore present at  $z_m$ , representing that range of compositions that crystallise in the lens.

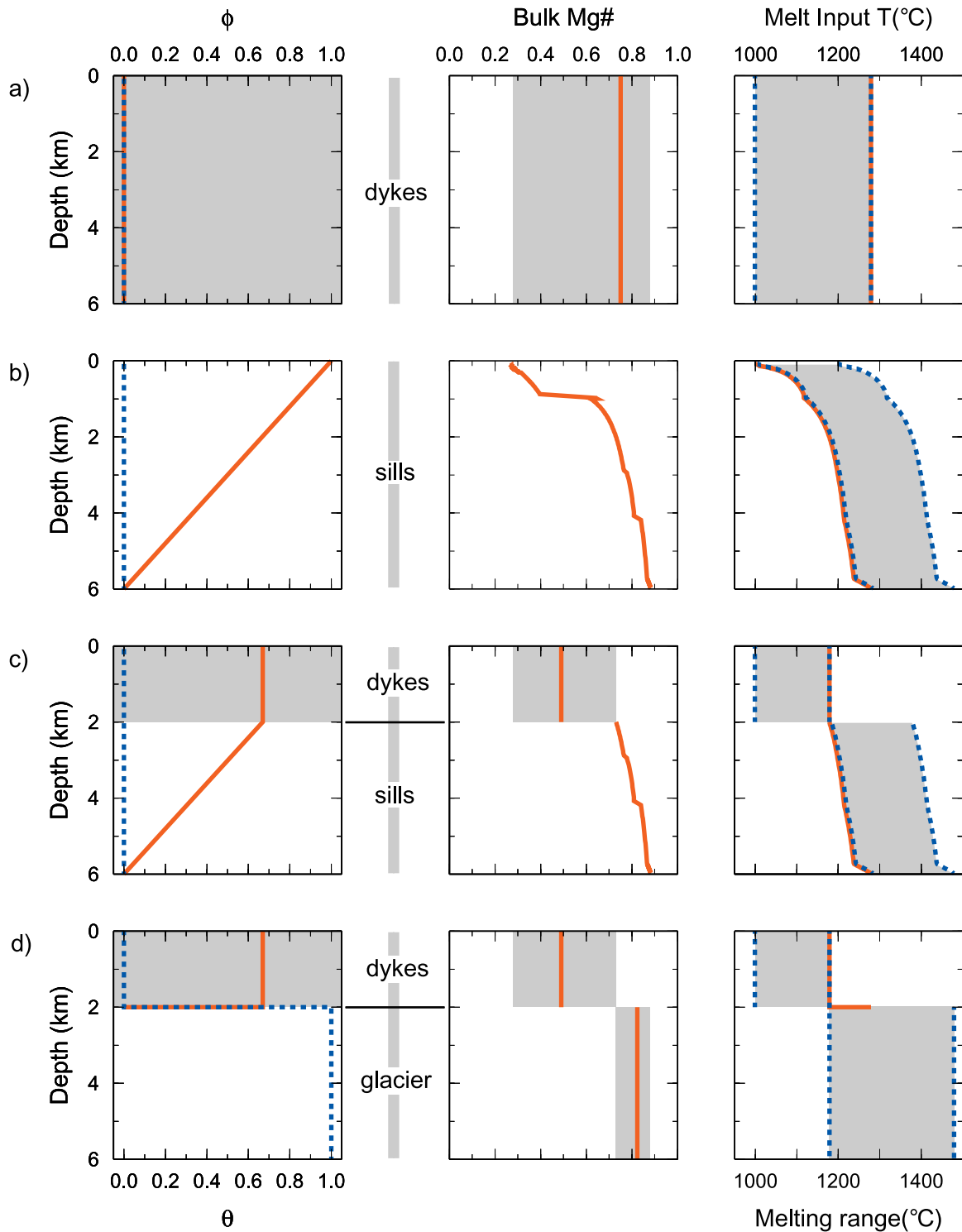
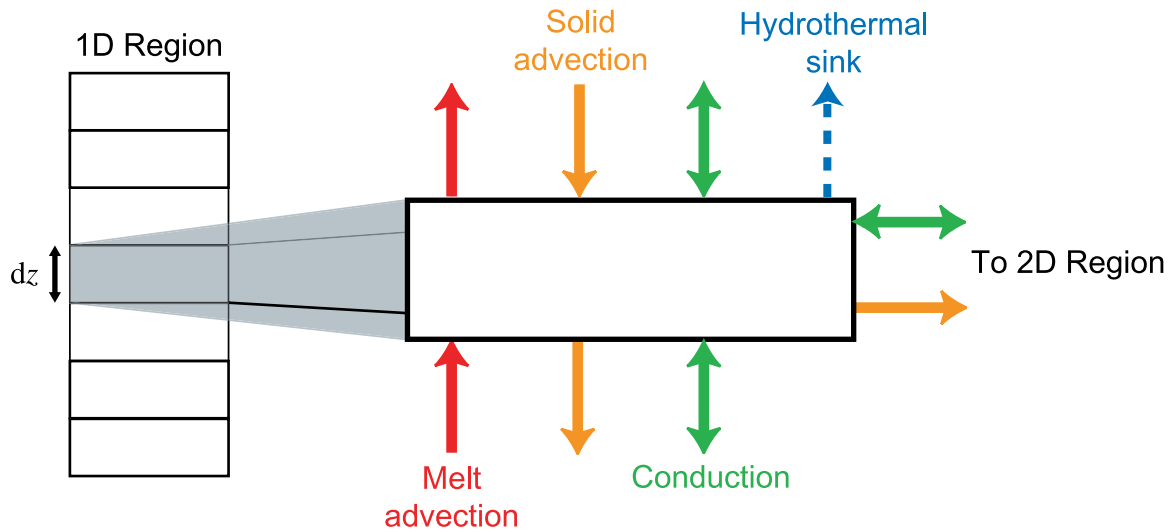


Figure 5.



**Figure 6.** Mass and thermal balance within the one-dimensional axial region. Advective terms, shown in orange and red, are included in the mass balance. Hydrothermal heat removal (for the upper crust), in blue, and conduction, in green, are also included in the thermal balance. Latent heat and specific heat is carried by the advective terms in the thermal balance. The balance is carried out for elements of infinitesimal height  $dz$ .

### 6.2.3. Hydrothermal Cooling

[30] The distribution of hydrothermal cooling is an important control on the calculated thermal structure. This cooling is included in the models as a series of heat sinks [Morton and Sleep, 1985]. Hydrothermal cooling is varied by changing the axial hydrothermal heat flux at the seafloor, the maximum off-axis hydrothermal heat flux at the seafloor and the decay length for off-axis cooling. Hydrothermal heat removal is treated in different fashions for on-axis and off-axis cooling. Heat removal in the axial region occurs over a temperature interval of 300–600°C, which is consistent with observed black smoker temperatures [Von Damm et al., 1985] and thermodynamic arguments [Jupp and Schultz, 2000]. The heat removal over this temperature interval is distributed as a cosine shaped bell, centered around 450°C, and the total depth integrated rate of heat removal per unit across axis area must be equal to a constant  $\hat{H}$  which is set in the modeling. In the off-axis region the distribution of heat sinks,  $H(x, z)$ , is chosen to be set in a slightly different way, which is described in detail in Appendix A. The maximum vertically integrated rate of heat removal is set at the axial edge of the off-axis region, and then decays exponentially away from this edge. The

vertical distribution of heat sinks is then chosen according to the calculated temperature and melt fraction within the axial region, so that the off-axis hydrothermal cooling is strongest where melt is present. The physical meaning of using heat sinks to model hydrothermal cooling has been discussed by Sleep [1991], and corresponds to time-averaged cooling where hydrothermal convection cells are not stable over long time periods and heat exchange does not occur between rising hydrothermal fluids and their surroundings.

## 6.3. Calculation of the Thermal Structure

### 6.3.1. Axial Region

[31] The thermal structure within the one-dimensional axial intrusion region is calculated using a mass and thermal balance. At each depth mass conservation is used to equate the vertical inflow of melt and solid to the vertical outflow of melt and solid and the horizontal outflow of material to the off-axis region. The horizontally outflowing material leaves the axial region with speed  $U$ , the half-spreading rate, at all depths. The vertical flow of material at crustal depths can be calculated once the distribution of crystallization,  $\theta(z)$ , has been specified, as shown in (1).

[32] A differential equation satisfied by the temperature structure,  $T(z)$ , in the one-dimensional axial intrusion region can be obtained from a thermal balance (Figure 6). Heat transport takes place by either conduction or advection (of both liquid and solid), while the crystallization of the crust releases latent heat, and hydrothermal circulation cools the crust by acting as a heat sink. Balancing the heat flows generated by these processes gives the differential equation for the temperature structure of the axial region.

[33] By balancing advection of heat by melt and solid, latent heat release during crystallization, and conduction and using the mass balance relationships in (1) gives the differential equation (5).

$$Ak \frac{d^2 T}{dz^2} - \rho c_p \mathcal{F}_s \frac{dT}{dz} + \rho L_h \mathcal{F}_s \frac{dT}{dz} \frac{d\gamma}{dT} - \rho c_p U(1 - \theta) T = \rho c_p \mathcal{F}_l \frac{dT_i}{dz} - \rho c_p U(1 - \theta) T_i - \rho L_h U \sigma(1 - \theta) - k \left. \frac{\partial T}{\partial x} \right|_A. \quad (5)$$

This equation must be solved in order to determine the temperature structure  $T(z)$  within the lower axial crust, where it is assumed that no hydrothermal heat removal takes place. The parameters and variables that feature in this equation are listed in Tables 1 and 2 while its derivation is given in Appendix B. The first term on the left hand side corresponds to vertical conduction, while the last on the right hand side is horizontal conduction of heat to the off-axis region. The other terms involving the melt and solid fluxes,  $\mathcal{F}_l$  and  $\mathcal{F}_s$ , and the half-spreading velocity,  $U$ , account for the advection of latent and specific heat both vertically within the axial region and horizontally to the off-axis region. Evaluation of the function  $T_i$ , the melt input temperature, and the crystal fractions  $\gamma$  and  $\sigma$  is outlined in section 6.4.

[34] In the upper crust, at depths shallower than  $z_m$ , hydrothermal circulation can act to cool the crust, providing an additional term in the heat balance. For all models considered later on in the paper, it is furthermore assumed that in the upper crust the vertical solid flux is zero, and the fluid intrusion temperature is constant ( $T_i^0$ ), as is expected for emplacement of the upper crust in dykes or lava

flows. Under these assumptions, the temperature equation for the upper crust is given by

$$Ak \frac{d^2 T}{dz^2} - U \rho c_p T = -U \rho (c_p T_i^0 + \tau L_h) - k \left. \frac{\partial T}{\partial x} \right|_A + AH, \quad (6)$$

with the hydrothermal cooling incorporated in the final term on the right hand side, and the crystal fraction  $\tau$  evaluated as described in section 6.4.

[35] In calculation of the temperature structure of the mantle it is assumed that the input temperature gradient is that which results from melting that produces a crustal thickness of  $z_c$  [McKenzie and Bickle, 1988]. This gradient is then matched to the melt input temperature at the onset of crystallization. The temperature equation used for the mantle is then derived by a heat balance which neglects vertical motion of melt and solid, and instead assumes that melt is supplied rapidly to the Moho at the ridge axis, giving

$$Ak \frac{d^2 T}{dz^2} - U \rho c_p T = -U \rho [c_p T_i + (\tau - 1) L_h] - k \left. \frac{\partial T}{\partial x} \right|_A. \quad (7)$$

The effect of the melt extraction style on mantle temperatures has been studied by Asimow [2002] who showed that varying the steady state melt extraction mechanism can lead to variation in the Moho temperatures of up to 20°C.

[36] In the models which simulate focused crystallization in a shallow melt lens the depth of the lens is set to be  $z_m$ . The crystallization and cooling that takes place at this depth acts as a source of heat and must be accounted for in the models. Heat is brought into the melt lens by liquid at temperature  $T_l(z_m)$ , with flux  $-\mathcal{F}_l(z_m)$ , and is removed upward from the melt lens by liquid with temperature  $T_i^0$ , and flux  $U z_m$ . Solid flows downward from the melt lens with flux  $\mathcal{F}_s(z_m)$ , temperature  $T(z_m)$  and crystal fraction  $\gamma(T(z_m))$ . The rate of heat release in the melt lens is calculated from the change in latent and specific heat carried into and out of the lens, and is thus given by

$$- \rho c_p \mathcal{F}_l(z_m) T_l(z_m) - \rho c_p U z_m T_i^0 - \rho c_p \mathcal{F}_s(z_m) T(z_m) + \rho L_h \mathcal{F}_s(z_m) \gamma(T(z_m)). \quad (8)$$

The heat source can be taken into account by adding a delta function of this size acting at  $z_m$  as a source term to the differential equation for temperature.

[37] Equations (5), (6) and (7) provide a second order differential equation that  $T(z)$  satisfies at all depths. Once the style and distribution of crystallization,  $\phi(z)$  and  $\theta(z)$ , have been specified, the equations can be solved, using a numerical relaxation scheme described in Appendix C, for a depth range  $0 < z < z_g$  (where  $z_g$  is the depth to the bottom of the mantle melting region), subject to the boundary conditions  $T(z_g) = T_f(z_g)$  and  $T(0) = 0$ . This relaxation scheme has the advantages of being rapid and allowing resolution of features of vertical extent of 10 m or less, in contrast to the numerical cost and low resolution of previous finite difference [Henstock *et al.*, 1993] or finite element [Phipps Morgan and Chen, 1993] models.

### 6.3.2. Off-Axis Region

[38] In the off-axis region the temperature field  $T(x, z)$  satisfies an advection-diffusion equation, with a constant horizontal advection velocity  $U$  [Sleep, 1975; Morton and Sleep, 1985]:

$$U \frac{\partial T}{\partial x} - \kappa \left( \frac{\partial^2 T}{\partial x^2} + \frac{\partial^2 T}{\partial z^2} \right) = H(x, z) - Q(T, z). \quad (9)$$

The two source terms on the right hand side of this equation represent heat removed by hydrothermal circulation and latent heat released by crystallization. Equation (9) is solved in the region  $x \geq A$ ,  $0 \leq z \leq z_l$ , where  $z_l$  is a depth at which isotherms are approximately horizontal. The boundary conditions that are applied are that: (1)  $T(A, z)$  matches the temperature structure found from the one-dimensional calculation in the axial region; (2)  $T(x, 0) = 0$ ; (3)  $T(x, z_l) = T_l$ , where  $T_l$  is the temperature in the axial region at depth  $z_l$ ; (4)  $T \rightarrow T_l/z_l$  as  $x \rightarrow \infty$ , so that far from the ridge the temperature approaches a conductive profile.

[39] Latent heat is assumed to be released uniformly as crystallization proceeds, so that  $Q(T, z)$  is given by

$$Q = \frac{UL_h}{c_p} \frac{\partial \tau}{\partial x}. \quad (10)$$

The nature of  $Q$  means that (9) is nonlinear, and so it is solved using an iterative scheme of the form

$$U \frac{\partial T_j}{\partial x} - \kappa \left( \frac{\partial^2 T_j}{\partial x^2} + \frac{\partial^2 T_j}{\partial z^2} \right) = H(x, z) - Q(T_{j-1}, z). \quad (11)$$

At each stage of the iteration the right hand side of this equation becomes a known function  $\hat{Q}(x, z)$ . In a similar fashion to the treatment of Morton and Sleep [1985], each inhomogeneous equation in the iterative scheme is solved by the use of a Fourier sine series expansion

$$T_j(x, z) = \frac{T_l z}{z_l} + \sum_{m=1}^{\infty} f_m(x) \sin\left(\frac{m\pi z}{z_l}\right), \quad (12)$$

as explained in Appendix D. In order to join the axial and off-axis regions, it is necessary to use another iterative scheme. The temperature in the axial region was calculated and then used as the boundary condition  $T(A, z)$  for the off-axis region. The resulting temperature field for the off-axis region was then used to calculate the horizontal heat conduction at  $x = A$ , which is used as an input for the axial calculation. Convergence of this scheme usually takes two or three iterations.

## 6.4. Composition, Input Temperatures and Melt Distribution

[40] A crucial part of the model formulation is the incorporation of petrological variation. After having defined the input variables  $\theta(z)$ ,  $\phi(z)$  and  $H(x, z)$  in section 6.2 and the equations used to calculate the thermal structure in section 6.3, we now describe how the compositional structure of the crust can be determined from  $\theta(z)$  and  $\phi(z)$ , and how this compositional structure and the temperature field are used to calculate the melt distribution within the crust. Knowledge of the relationship between melt temperature, extent of crystallization and the composition of the melt and the crystallizing solids is also required for calculation of the thermal structure due to the presence of the melt input temperature,  $T_i$ , in (5) and (6).

### 6.4.1. Compositional Structure

[41] All crustal solids are taken to be formed as the products of fractional crystallization, and it is thus

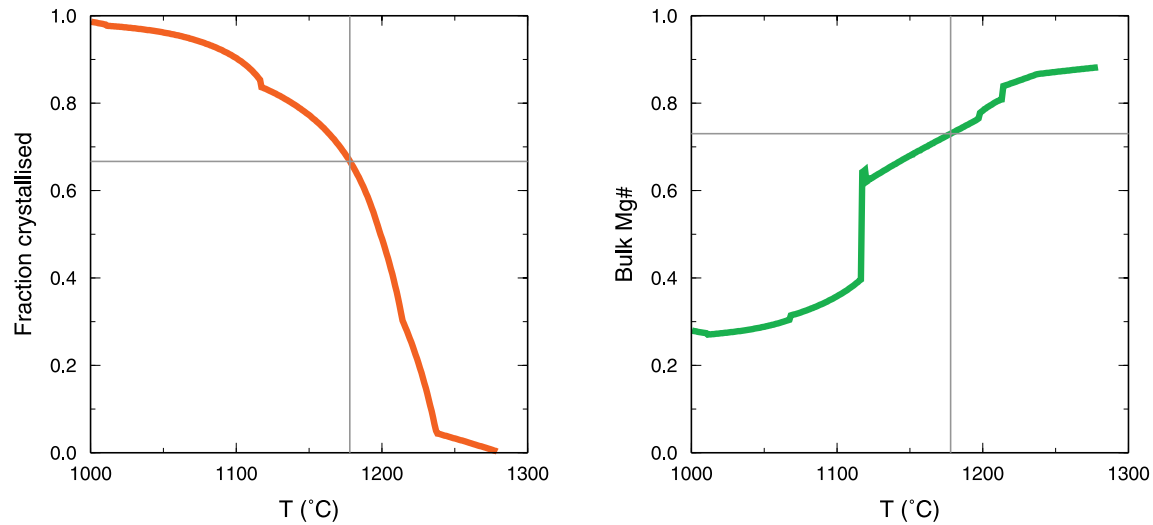


**Figure 7.** Results of a MELTS fractional crystallization model for an estimated primary mantle melt composition. (a) The accumulated fraction crystallised as a function of temperature. (b) Bulk Mg# of the instantaneous products of fractional crystallization at any temperature. The large drop in Mg# just above 1100°C is caused by iron-rich oxides joining the liquidus assemblage. The composition of the primary mantle melt used was that of KG1 given by *Korenaga and Kelemen* [1997] calculated for 14% polybaric incremental batch accumulated melting of depleted mantle [*Kinzler and Grove*, 1992]. The composition in wt% oxides is: SiO<sub>2</sub> 49.0; TiO<sub>2</sub> 0.88; Al<sub>2</sub>O<sub>3</sub> 16.8; FeO 7.85; MgO 11.6; CaO 11.9; Na<sub>2</sub>O 1.92; K<sub>2</sub>O 0.05. The model oxygen fugacity was set at 1 log unit beneath the fayalite-quartz-magnetite buffer and the pressure of crystallization was set at 0.1 GPa, equivalent to a depth of about 3 km. Increasing the crystallization pressure increases the temperature of the onset of crystallization by less than 10°C. The grey lines show the temperature and composition reached after 67% crystallization of the initial mantle melt.

important to understand the compositional evolution during fractional crystallization of a primary mantle melt. This behavior can be calculated using the MELTS algorithm [*Ghiorso and Sack*, 1995; *Asimow and Ghiorso*, 1998], and the results of a calculation for fractional crystallization is shown in Figure 7. The calculation shows the fraction of melt crystallized as a function of temperature, together with the evolution of the composition of solid products of crystallization as a function of the extent of crystallization.

[42] The composition only varies with depth in the models, and can be calculated using the style and distribution of crystallization and the relationship in Figure 7b. For sills style crystallization, the bulk composition of the solid formed at  $z$  is the instantaneous composition of the product of fractional crystallization after the appropriate extent of fractional crystallization of the primary melt. Therefore the composition is controlled by  $\phi(z)$ , and can be evaluated directly using the relationship in Figure 7b. Where dyke style crystallization occurs

there is no further large scale separation of melt and solid, so the bulk composition of the final solid is the same as that of the melt that was originally intruded (Figure 4). This composition is a function of the  $\phi(z)$  of the melt at the depth of intrusion. During the fractional crystallization of this trapped melt at depth  $z$  the composition of the crystallizing material may vary. If local chemical separation of melt and solid occurs, as in closed system fractional crystallization, then a range of compositions from that expected for  $\phi(z)$  through to that expected for the final increment of crystallization (Figure 7b) may be generated on a scale of millimeters to meters.

[43] When crystallization is focused at  $z_m$  then the composition of the material that is fed downward from the lens can be calculated if the extent that melt has crystallized when it enters the melt lens,  $\phi_0$ , and the extent of crystallization when melt leaves the lens to supply the upper crust,  $\phi_1$ , are known. These terms can be calculated from  $\theta(z)$  as described in section 6.2.2. Therefore the range of

compositions in the solid material fed downward from the lens will be from that produced at  $\phi_0$  through to  $\phi_1$ , and the bulk composition can be calculated from a weighted average of these compositions. When this material is fed downward the average composition of the material at any depth can be calculated from  $\theta(z)$  and the composition both of the material produced in sills in the lower crust and of that generated in the melt lens. Both the bulk composition and the range resulting from a number of different  $\phi(z)$  and  $\theta(z)$  are shown in Figure 5.

### 6.4.2. Melt Input Temperatures

[44] A knowledge of  $\phi(z)$  allows the calculation of the melt injection temperature,  $T_i(z)$ . If a fraction  $\phi$  of the crust has crystallized below a given depth, then the input temperature at that depth will correspond to the temperature of the melt after a fraction  $\phi$  of the original mass of primary mantle melt has been solidified during fractional crystallization. The melt input temperature is thus given by

$$T_i(z) = T_f(\phi(z)), \quad (13)$$

where  $T_f(\phi)$  is the fractional crystallization curve shown in Figure 7a.

### 6.4.3. Distribution of Melt

[45] The melt fraction present within the crust can also be calculated with a knowledge of  $\phi(z)$ . For material that undergoes dyke style crystallization the melting behavior will be determined by the  $T_f(\phi)$  fractional crystallization curve shown in Figure 7a. Material that has already undergone a fraction  $\phi_D$  of crystallization will be completely molten at temperatures above its input temperature,  $T_f(\phi_D)$ , and will be completely solid at temperatures below  $T_f(1)$ , the melting temperature of the composition with the lowest melting point. The crystal fraction of this material is therefore given by

$$\tau(T, z) = \begin{cases} 0 & T > T_f(\phi_D), \\ 1 & T < T_f(1), \\ \frac{\phi_T - \phi_D}{1 - \phi_D} & \text{Otherwise,} \end{cases} \quad (14)$$

where  $T_f(\phi_T) = T$  for  $T_f(1) < T < T_f(\phi_D)$ .

[46] When sills style crystallization takes place at a given depth, the material added to the crust at this depth has the composition of the solid residue of fractional crystallization. This material has different melting and crystallization behavior to that of the melt that separates (Figure 2). The compositions and remelting behavior of the solid residues of fractional crystallization were calculated using MELTS. The residues of fractional crystallization are, as expected, solid at the temperature of melt separation, and have a melting interval of 60–600°C. For simplicity, we model the melting behavior of the solid residues of fractional crystallization with a linear melting interval,  $M$ , of 200°C starting from fully solid at  $T_i$  for the depth of interest, so that the crystal fraction of the residues,  $\sigma$ , is given by

$$\sigma(T, z) = \begin{cases} 1 & T < T_i, \\ 1 - (T - T_i)/M & T_i < T < T_i + M, \\ 0 & T > T_i + M. \end{cases} \quad (15)$$

Note that  $\sigma(T, z)$  is implicitly a function of composition because  $T_i$  is defined as a function of  $\phi$  in (13). When generation of the lower crust takes place via crystallization at  $z_m$ , as in Figure 5d, the melting behavior is modelled by considering that the solid residues of fractional crystallization were generated over a range of temperatures and  $\phi$ . In order to calculate the remelting behavior of this material the following average over the compositions that crystallize in the melt lens must therefore be used:

$$\gamma(T) = \frac{1}{\phi_1 - \phi_0} \int_{\phi_0}^{\phi_1} \sigma(T, z) d\phi. \quad (16)$$

[47] The melt fraction within the axial region also includes a contribution from melt flowing through the crust. This melt may not necessarily reach thermal equilibrium with its surroundings. An estimate of the corresponding contribution to the total melt fraction can be made by approximating the porosity required for this melt transport as

$$\psi = \frac{\mathcal{F}_l}{Aw}. \quad (17)$$

where  $w$  is the vertical melt transport velocity. The total melt fraction within the axial region is then given by

$$F = 1 - \tau + \psi, \quad (18)$$

while in the off-axis region the melt fraction is given by

$$F = 1 - \tau, \quad (19)$$

since there is no vertical motion of material in that region. It should also be noted that an equilibrium time-averaged melt fraction need not be present for melt to travel through the crust if melt supply is episodic (e.g., dyking events).

## 7. Model Results

[48] The flexibility and efficiency of the modeling method allowed the exploration of a wide range of parameters for several styles and distributions of crystallization, including many sills and gabbro glacier models. In the favored models, which are described here, the half-width of the one-dimensional axial intrusion region,  $A$ , is set at 1 km. This value was chosen to match the geophysical observations described in section 2. The half-width was kept constant with depth because the introduction of a depth varying  $A$  greatly increases the complexity of the models. The half-spreading rate,  $U$ , was set at  $60 \text{ mm yr}^{-1}$ , similar to that of the EPR in the  $9^\circ\text{N}$  region. A crustal thickness,  $z_c$ , of 6 km was used for all of the models, and  $z_m$ , the depth where crystallization can be focused in the models, is set at 2 km. The upward melt velocity within the crust,  $w$ , is set at  $50 \text{ m yr}^{-1}$ , in broad agreement with melt transport rates estimated from geochemical or geological arguments. [Kelemen *et al.*, 1997a; MacleNNan *et al.*, 2002].

### 7.1. Many Sills Models

[49] The results of a many sills model are shown in Figure 8. The distribution of crystallization is shown in Figure 5d, as is the resulting compositional structure. The compositional structure matches that observed for Oman (Figure 2) in that the lower crust is composed of the residues of fractional crystalliza-

tion, whereas the upper crust is compositionally variable but has an average composition similar to that of basaltic melt. The results of the modeling are also broadly consistent with the geophysical observations. A melt body is produced at 1–2 km depth and the melt fraction remains low in most of the axial lower crust save a region of >20% melt near the Moho. Despite the crystallization of the lower crust in sills in situ the lower axial crust has melt fractions between 0.3% and 10% apart from in a thin region at the Moho. This result shows that many sills models can be consistent with the geophysical observations, as long as the hydrothermal circulation can remove sufficient heat from the flanks of the axial region down to Moho depths. The effect of the hydrothermal cooling is to create high thermal gradients which allow significant conductive heat transfer out of the axial region. Thermal balance models, such as that in (B6), can be used to estimate that the horizontal thermal gradient at the edge of the axial region must exceed around  $2^\circ\text{C m}^{-1}$  in order for the axial lower crust to be solid.

[50] Horizontal variations in P wave velocity were calculated from the temperature and melt fraction using the method of *Dunn et al.* [2000], for the case where anelasticity is not important and melt occurs in spheres. This prediction gives the smallest P wave speed anomaly for variations in melt fraction or temperature. Variation in water depth was calculated using a simple one-dimensional water-loaded isostatic balance using a reference solid crustal density of  $2900 \text{ kg m}^{-3}$ , a reference melt density of  $2720 \text{ kg m}^{-3}$ , a reference mantle density of  $3200 \text{ kg m}^{-3}$  and a thermal expansion coefficient of  $3 \times 10^{-5} \text{ }^\circ\text{C}^{-1}$ . These isostatic variations in bathymetry are broadly consistent with the observations of ridge axis morphology, with bathymetric drops of 300–400 m occurring within 10 km of the ridge axis. However, due to flexural effects, it is unlikely that such isostatic models will be able to reproduce the detailed morphology observed at the EPR axis [Shah and Buck, 2003].

[51] The sensitivity of the many sills model to changes in the intrusion width and hydrothermal circulation can be investigated by varying parameters from those used to produce the model in Figure 8. These tests indicate that there is a strong

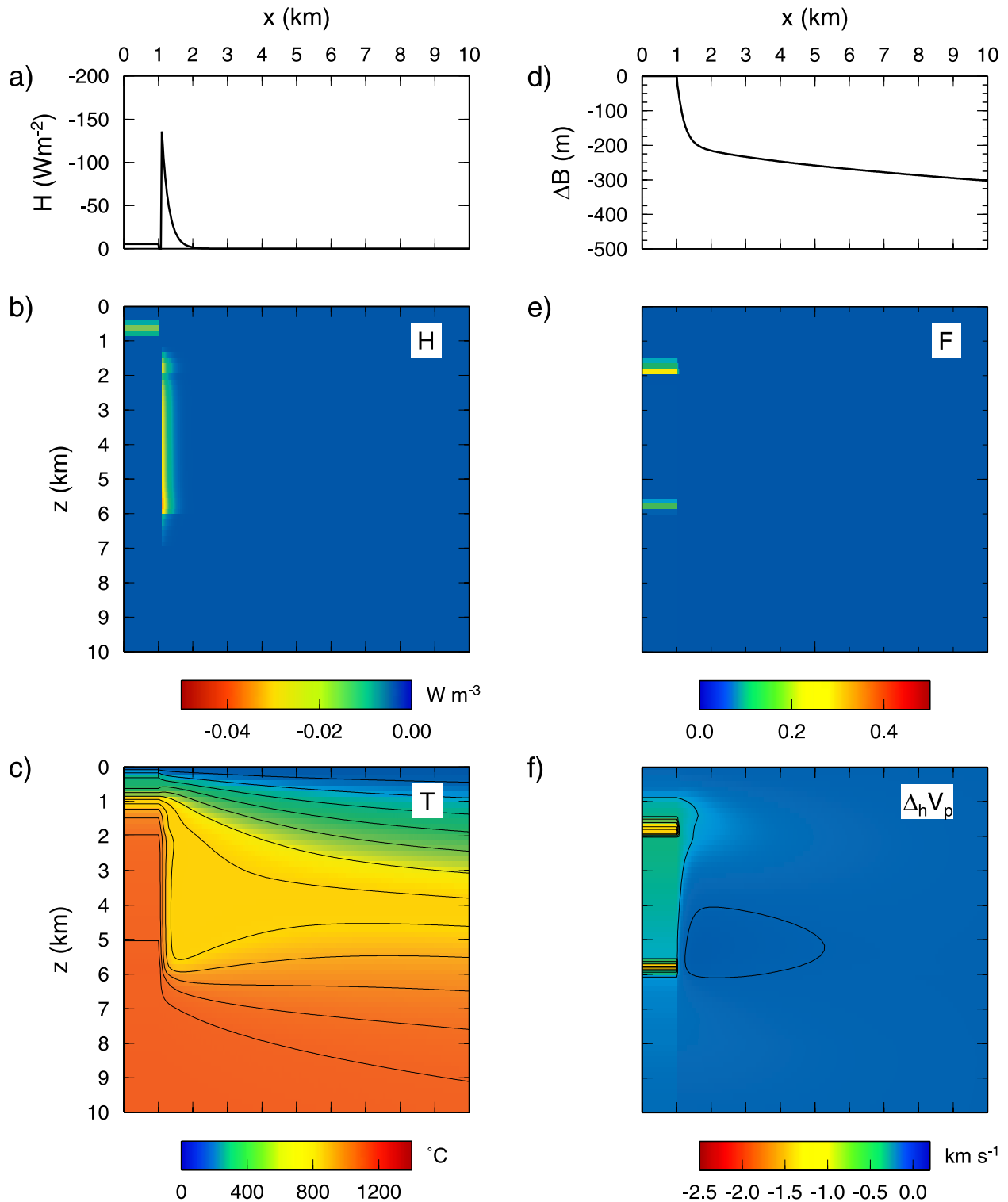


**Figure 8.** Many sills model using distribution of crystallization shown in Figure 5c and an axial intrusion region width of  $A = 1000$  m. (a) Vertically integrated heat removal due to hydrothermal circulation with  $\hat{H} = 5.6$   $\text{W m}^{-2}$ ,  $H_{\text{max}} = 120$   $\text{W m}^{-2}$ ,  $\lambda = 200$  m,  $\Delta = 100$  m. (b) Distribution of hydrothermal heat removal,  $H(x, z)$ , throughout the crust. (c) Temperature structure. (d) Bathymetric variation predicted using isostatic model. (e) Calculated melt fraction within the crust. (f) Horizontal P wave velocity anomaly predicted from temperature and melt fraction. See text for details.

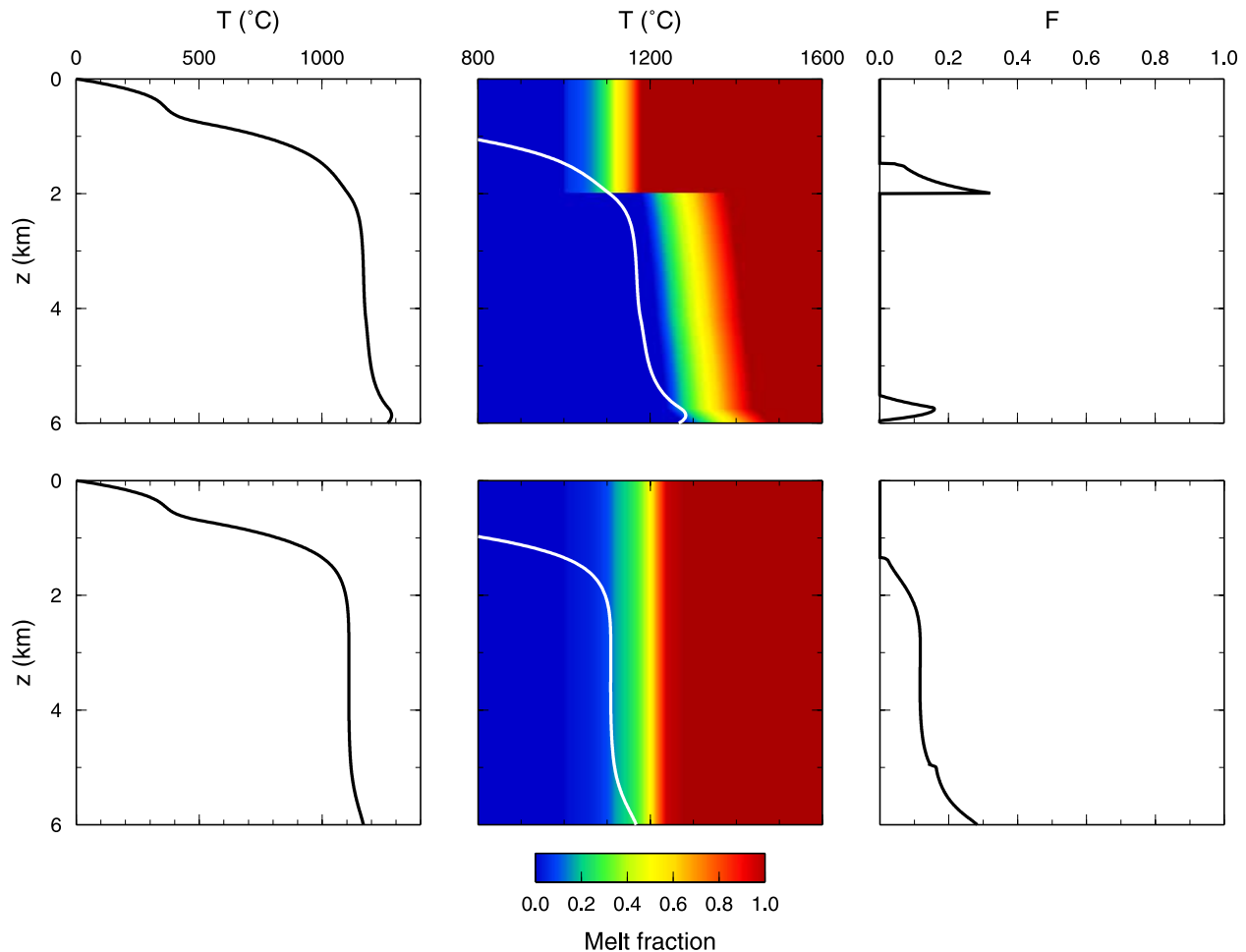


**Figure 9.** The results shown in the first row are for the crystallization distribution shown in Figure 5c with the hydrothermal circulation from Figure 8b. The first column shows axial temperature. The second column shows the axial temperature on a colour plot of melt fraction as a function of temperature and depth. The colour scale for melt fraction is shown at the base of the column. Melting behaviour changes with depth where crustal composition changes with depth. The third column shows the resulting distribution of melt. The results in the lower row are for the crystallization distribution in Figure 5a with the same distribution of hydrothermal cooling as for the upper row.

trade-off between the parameters, particularly the width of the axial intrusion region and the strength of on-axis hydrothermal cooling, and that it is possible to produce numerous many sills models that are broadly consistent with the geophysical and petrological observations. When the strength of hydrothermal cooling is increased, so that  $\dot{H}$  is over  $10 \text{ W m}^{-2}$ , no melt is present in the axial crust.

### 7.1.1. Petrological Variation and Generation of the Shallow Melt Lens

[52] The model generates a melt lens overlying a near-solid region because compositional variation

is present. Figures 5 and 9 show that this compositional step corresponds to a change in the remelting behavior of the crust. In Figure 9 the axial melt fraction from the sills model of Figure 8 is compared with that expected for the crystallization distribution in Figure 5a, where all of the crust forms by intrusion of dykes at the ridge axis. This figure highlights the role of petrological variation in generating the melt lens. While the temperature structures shown in Figures 9a and 9b are similar, the dyke model in Figure 9b is slightly cooler in the lower crust due to differences in the pattern of heat release. The major difference between the models is that of the remelting behavior. The sharp

step in the style of crystallization in the many sills model, which generates cumulate gabbros by fractional crystallization in the lower crust and trapped melt compositions in the upper crust, leads to a sharp step in the melting behavior. Thus a melt lens with a sharp base can be produced in the many sills model, in agreement with the seismic reflection observations. A second melt body forms near the Moho due to the difficulty of extracting heat from the lowermost axial crust and the high values of  $dT/d\phi$  at the onset of crystallization (Figure 5c) which enhances the specific heat release. In contrast, the dyke model in Figure 9b produces no petrological stratification so there are no steps in melting behavior and therefore no melt lens is produced.

[53] In previously published thermal models, where no compositional variation was allowed, the axial structure of melt lens overlying near-solid lower crust was produced by variations in temperature [Phipps Morgan and Chen, 1993; Henstock *et al.*, 1993]. A zone of high temperatures in the upper crust was thought to correspond to the shallow melt lens, and lower temperatures at greater depths produced a near-solid axial lower crust. In order to produce a transition zone of less than 100 m thickness between the melt lens and its near-solid floor, as inferred from seismic reflection results, it is necessary for either petrological variation or thermal gradients of  $1^{\circ}\text{C m}^{-1}$  or more to be present. Such gradients must be produced by extensive hydrothermal cooling in the region directly beneath the melt lens. None of the previous thermal models have reproduced such high thermal gradients. The results of our models that include petrological variation indicate that there is no need for decreasing temperatures with depth or extensive hydrothermal circulation beneath the melt lens in order to produce a thin shallow melt lens overlying a near-solid lower crust.

## 7.2. Gabbro Glacier Models

[54] The results of a model of crustal accretion where all the lower crust forms in the shallow melt lens are shown in Figure 10. This model result shows a thin shallow melt lens overlying a near-solid axial lower crust, in agreement with the geophysical observations. The distribution and

style of crystallization,  $\phi$  and  $\theta$ , for this model were taken from Figure 5d and result in a compositional stratification that resembles that observed in Oman. Both many sills and gabbro glacier models can therefore match the large-scale geophysical and petrological observations.

[55] The predicted melt fraction shows the presence of a thin melt lens formed at the depth where focused crystallization takes place. The molten region with over 10% melt has a thickness of about 120 m, and a very small region of pure melt is present at the center of the region. While the upper boundary corresponds to a region of high geothermal gradient caused by the balance between hydrothermal heat removal and latent heat release, the lower boundary reflects a compositional change. The form of this melt lens is similar to that inferred to exist from seismic reflection studies, while the melt bodies of over 1 km thick predicted from the sills models of Figure 8 are much larger than those observed on the EPR. The lower axial crust in the gabbro glacier model of Figure 10 contains between 1% and 5% melt.

[56] The distribution of hydrothermal heat removal used in this model is very different to that shown in the sills model of Figure 8. In the gabbro glacier model of Figure 10 over 50% of the total hydrothermal heat loss takes place above the shallow melt lens, while in the many sills model this figure is 18% because the bulk of the hydrothermal cooling takes place in the flanks of the axial region. These differences reflect the amount of latent heat that must be removed from the upper crust; in the many sills model only a third of the total latent heat is released in the upper crust, while in the gabbro glacier model all of the latent heat release takes place there. While a number of different distributions of hydrothermal cooling can produce gabbro glacier models that are broadly consistent with the geophysical observations, the difference in the distribution of hydrothermal heat removal between successful many sills and gabbro glacier models is robust. If the value of  $\hat{H}$  is increased to  $26.4 \text{ W m}^{-2}$  in the gabbro glacier model of Figure 10 then the shallow melt lens disappears, but when  $\hat{H} = 16.4 \text{ W m}^{-2}$  or less the melt lens thickness is greater than 1.5 km.

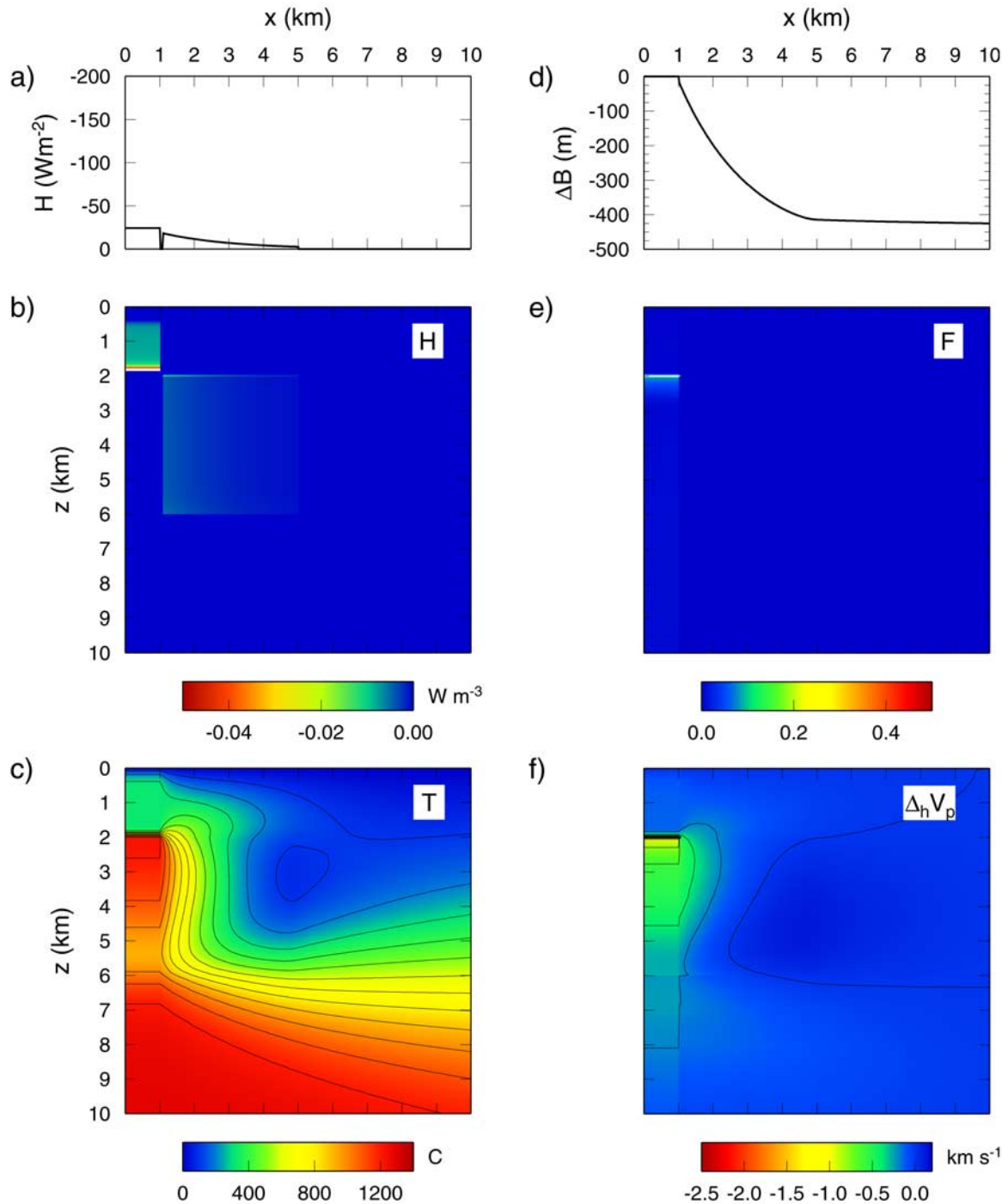


**Figure 10.** Gabbro glacier model using distribution of crystallization shown in Figure 5d and an axial intrusion region width of  $A = 1000$  m. Vertically integrated heat removal due to hydrothermal circulation with  $\hat{H} = 24.4$   $\text{W m}^{-2}$ ,  $H_{\text{max}} = 18$   $\text{W m}^{-2}$ ,  $\lambda = 2000$  m,  $\Delta = 100$  m. Arrangement of plots as for Figure 8.

[57] The gabbro glacier model of Figure 10 shows no second melt lens at the Moho. In order to produce an increase in melt fraction toward the bottom few hundred meters of the crust it is necessary to restrict the vertical range of off-axis

hydrothermal cooling to the upper half of the lower crust. For instance, if  $\hat{H} = 20.4$   $\text{W m}^{-2}$  and off-axis circulation is restricted to the top 3 km with  $H_{\text{max}} = 6$   $\text{W m}^{-2}$  then a zone of 200 m height with melt fractions of over 20% can be produced at the base

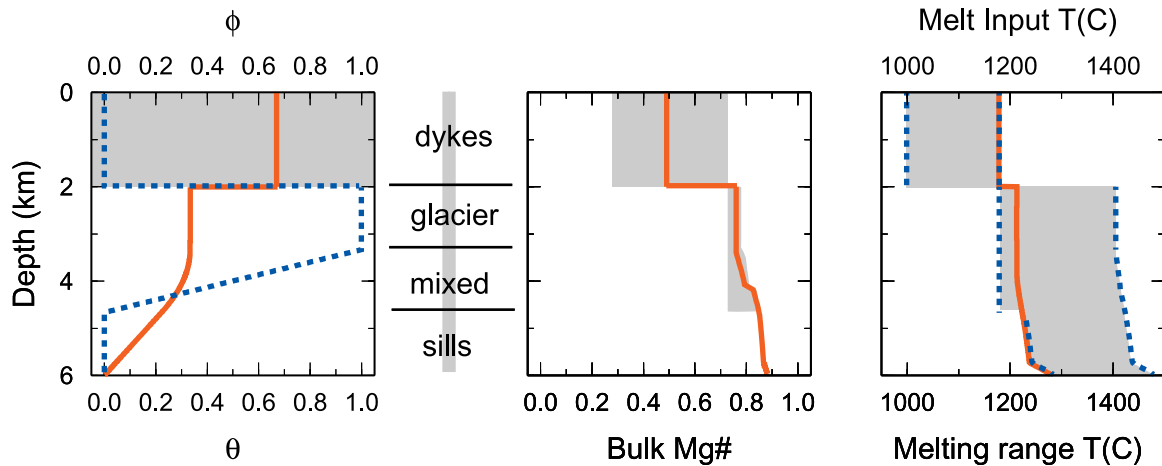


**Figure 11.** Distribution of crystallization in the hybrid model. Symbols are the same as those for Figure 5.

of the crust. However, this zone has much broader boundaries than the lower crustal melt lens shown in Figure 8 and the transition zone between 15% melt and 20% melt is over 500 m thick in contrast to the 100 m thick zone in the sills model. The cause for the difference in thickness is that higher thermal gradients exist near the Moho of the sills models than that of the gabbro glacier model.

### 7.3. Hybrid Models

[58] Both many sills and gabbro glacier models can broadly match the geophysical observations of melt distribution at active ridges and the petrological structure observed in Oman and inferred for the EPR. However detailed geophysical observations, such as the form of the shallow melt lens and its boundaries, or the presence of a near-Moho melt body, are not both easily reproduced using these extreme models. Furthermore, the textural variations in the Oman gabbros have been attributed to the operation of hybrid crustal accretion mechanisms where part of the lower crust is generated in a gabbro glacier fed by the shallow melt lens and the rest forms in the lower crust [Boudier *et al.*, 1996]. The many sills accretion model proposed by Kelemen *et al.* [1997b] that is shown in Figure 1b also involves a limited amount of downward solid subsidence in the uppermost part of the lower crust. In order to investigate this proposal a number of hybrid models were run to determine the details of the melt distribution when the proportion of the

lower crust that is formed in the shallow melt lens varies as a function of depth.

[59] The distribution of crystallization for an example of a successful hybrid model is shown in Figure 11, and the model results are shown in Figure 12. In this model the lower third of the lower crust is produced by crystallization in situ, and the top third of the lower crust is all made in a gabbro glacier. The middle third forms a transition zone between these two mechanisms. The model results show that an upper melt lens of 180 m thickness is produced with a near-solid roof and floor, that melt fractions are between 1% and 10% in much of the lower axial crust and that a 200 m thick Moho melt body is generated. This hybrid model not only produces the large-scale geophysical observations of a shallow melt lens overlying a near-solid lower crust but also more detailed observations such as the melt lens thickness and the presence of a Moho melt body. Pure gabbro glacier models cannot recreate realistic Moho level melt bodies, while pure many sills models produce thick shallow melt lenses. Hybrid models therefore provide better matches to the geophysical observations than the pure gabbro glacier or many sills models.

[60] A number of hybrid models were run in order to constrain the proportion of the lower crust that must crystallize in the shallow melt lens in order to maintain a lens that is of similar thickness to those inferred by seismic reflection studies. The thickness of the lens and its upper boundary are con-

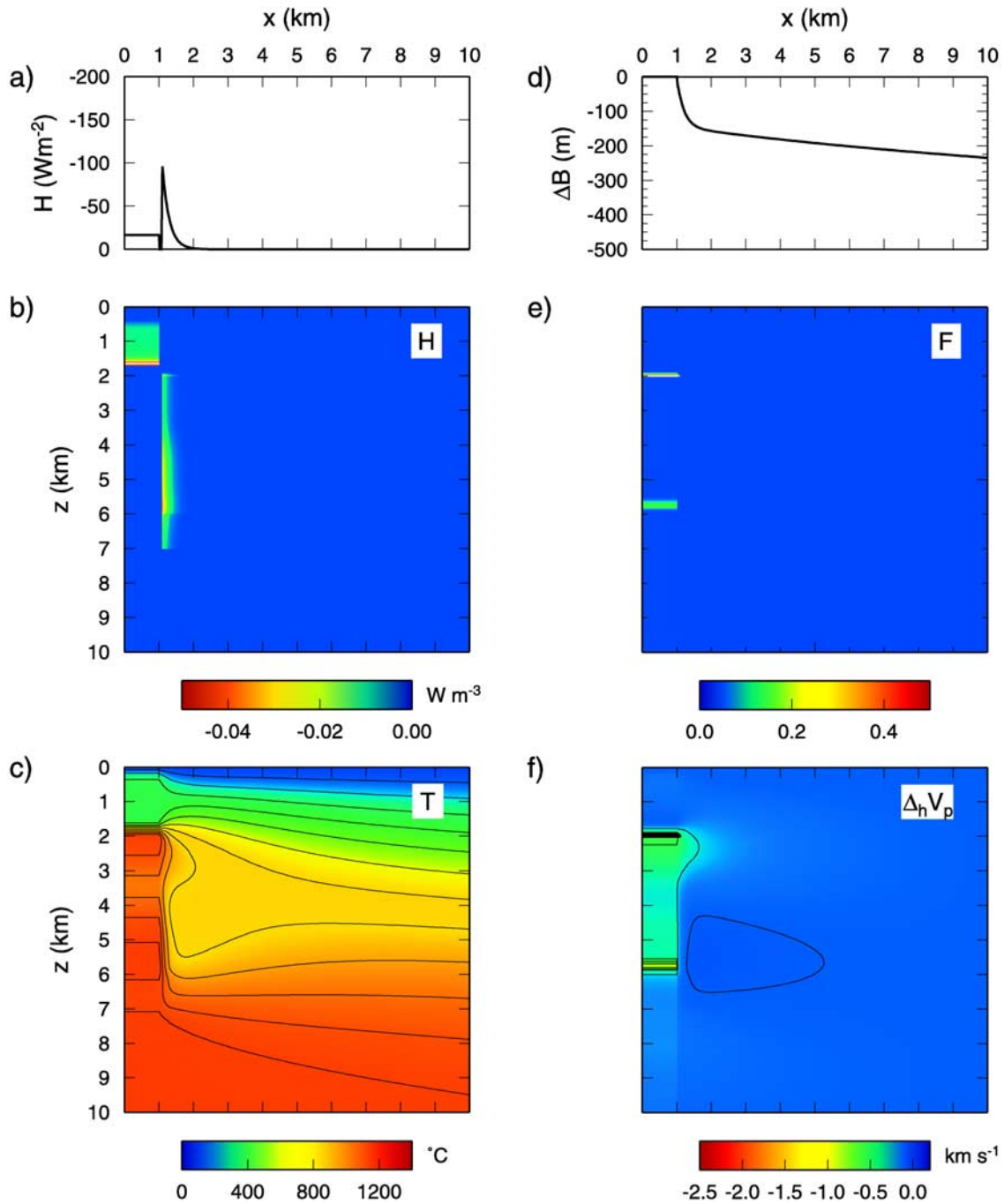


**Figure 12.** Hybrid model using the distribution of crystallization shown in Figure 11 and an axial intrusion region width of  $A = 1000$  m. Vertically integrated heat removal due to hydrothermal circulation with  $\bar{H} = 16.4 \text{ W m}^{-2}$ ,  $H_{\text{max}} = 85 \text{ W m}^{-2}$ ,  $\lambda = 200$  m,  $\Delta = 100$  m. Arrangement of plots as for Figure 8.

trolled by the thermal gradients within the model, which is determined by the balance between latent heat release and hydrothermal heat loss in the region above the melt lens [Lister, 1995; Chenevez and Nicolas, 1997]. For steady state models the thickness of the conductive boundary layer above

the lens is inversely proportional to the strength of hydrothermal heat removal. When less than about 1/4 of the lower crust is formed in the shallow melt lens the predicted thermal gradients are not high enough to produce a melt lens with over 25% melt and a thickness of under 250 m.

[61] These models do not include the heat transfer that is likely to be caused by convective motions within the melt lens, nor by stoping of the roof of the lens [Coogan *et al.*, 2003]. Since convection generates higher heat flow through the top of the melt lens its presence will encourage the formation of a small melt lens with thin boundaries. It may therefore be possible to reproduce the geophysical observations with less than 1/4 of the lower crust forming in the shallow melt lens. The deeper melt body that has been observed near Moho depths can be reproduced in models when the lowermost 800 m of the crust forms by crystallization in sills at the base of the crust.

[62] These results indicate not only that hybrid models of crustal accretion can account for some of the more detailed geophysical observations from the EPR but also that a wide range of hybrid models are permitted. Models where between 25% and 75% of the lower crust forms by crystallization in the shallow melt lens certainly provide a successful match to both the large-scale and detailed geophysical observations, and our limited understanding of the nature of convection in magma chambers and of the details of the distribution of melt in the melt lens [Ponce-Correa *et al.*, 1999] and Moho region means that an even wider range of models may be permitted.

## 8. Discussion

### 8.1. Models and Observations of Hydrothermal Cooling

[63] The model results show that both many sills and gabbro glacier models can reproduce the broad scale geophysical observations from the EPR and petrological observations from Oman. However, this agreement is strongly dependent on the distribution of hydrothermal heat removal from the crust, which was varied in order to reproduce the observations. In the case of the many sills or hybrid models it is necessary to remove heat from the flanks of the axial intrusion zone right down to Moho depths in order to produce a distribution of melt that is consistent with the geophysical observations. In the models shown in Figures 8 and 12 the heat removal in the off-axis lower crust takes

place over a range of temperatures between 600 and 900°C. These temperatures are higher than those of black smoker fluids but are in agreement with geochemical estimates of the temperature of formation of hydrothermal mineral veins in both ophiolite sections and oceanic crust [Gillis, 1995; Manning *et al.*, 1996; Coogan *et al.*, 2002b; Nicolas *et al.*, 2003]. A direct numerical simulation of hydrothermal flow has been used by Cherkaoui *et al.* [2003] in order to examine cooling behavior. When their model permeability exceeds about  $4 \times 10^{-14}$  m<sup>2</sup> then hydrothermal circulation cools the entire crust efficiently and produces almost vertical isotherms in the lower crust, similar to those shown in Figures 8 and 12. Their model results show that when the lower crust is cooled in the flanks of the intrusion zone then the ratio of advective (hydrothermal) to conductive heat flux at the seafloor within 12 km of the ridge axis is approximately 10. The ratio of hydrothermal heat loss to conductive heat loss in the successful models shown in Figures 8, 10, and 12 is between 3 and 7. The differences between these values and those of Cherkaoui *et al.* [2003] are likely to be due to the incorporation of petrological variation and a finite-width intrusion zone in our models.

### 8.2. Limitations of the Modeling Scheme

[64] As previously noted, the solid and melt flow in our models is extremely simple (section 6.1). Dynamical models of flow at the ridge axis have been developed by Chenevez *et al.* [1998], who were able to successfully reproduce the flow field inferred from geological markers of strain in the Oman ophiolite. The simplicity of the flow field in our models prevents them from matching such observations. More generally, our models do not include any of the dynamics of flow which must ultimately govern the relative movement of melt and solid in the crust and the nature of the hydrothermal flow. The geometry of our problem is specified, including the depth of the melt lens, so we cannot make predictions about this depth. Rather, we seek to find models that are consistent with both geophysical observations from ridges and the large scale petrological stratification observed in ophiolite crust. A further type of observation that our models cannot match in detail is

that of small-scale compositional variation that has been found in gabbros from Oman [Korenaga and Kelemen, 1997; Coogan *et al.*, 2002c]. The models cannot reproduce such observations because at present liquids of more than one composition cannot coexist at the same depth in the axial region of the model. Our many sills models also show a monotonic drop in the Mg# of the gabbros with decreasing depth, while the many sills model of Kelemen *et al.* [1997b] involves layering because a finite extent of crystallization takes place in sills of finite height before the melt is fed to higher levels. In common with previous models, we have made no attempt to model time dependent or three dimensional effects.

### 8.3. Future Observational and Modeling

[65] The present modeling scheme and the observations used here do not place strong constraints on the proportion of the lower crust that forms by crystallization in the shallow melt lens. A number of observational and modeling techniques may provide stronger constraints on the cooling and crystallization, including measurements of hydrothermal heat flow [Baker *et al.*, 1996], studies of the composition of vent fluids [Von Damm *et al.*, 1985], isotopic studies of altered crustal rocks [Teagle *et al.*, 2003], petrological estimates of the temperatures of hydrothermal vein formation in the lower crustal gabbros [Coogan *et al.*, 2002b; Nicolas *et al.*, 2003], and textural studies of these gabbros [Boudier *et al.*, 1996; MacLeod and Yaouanq, 2000]. Below we discuss three additional techniques that may be incorporated into our modeling framework in a straightforward fashion to provide further information about the crustal accretion processes.

[66] Petrographic [Garrido *et al.*, 2001] and petrological [Coogan *et al.*, 2002a] observations from Oman gabbros have been used to estimate their cooling rates. Both of these studies have shown that cooling rates decrease with depth in the crust, but at present the technique only permits study of relative variations in cooling rate.

[67] A number of studies have shown that the axial bathymetric and gravity structure of fast spreading

mid-ocean ridges can be used to investigate the cooling behavior of the crust [Cochran and Buck, 2001; Shah and Buck, 2001, 2003]. In particular, Shah and Buck [2003] developed a mechanical model of a ridge axis with a simple thermal structure, and found that their model results best matched the observed bathymetric profile when hydrothermal cooling penetrated the lower crust within 2 km of the ridge axis.

[68] At present three-dimensional (3-D) seismic tomography models provide weak constraints on the porosity of the axial lower crust, the size of the melt pockets and the width of the low velocity zone. Detailed studies of the form of the shallow melt lens have been carried out using seismic reflection data and such studies provide constraints on the degree of focussing of melt into the shallow melt lens. However, this kind of analysis has only been applied to data from a limited number of locations. A better knowledge of the distribution of melt at the axial crust, and therefore the crustal accretion process, may be achieved by carrying out 3-D wide-angle and reflection seismic surveys in tandem with compliance and controlled source electro-magnetic measurements, and by objective modeling of the data.

## 9. Conclusions

[69] Thermal models of oceanic crustal accretion incorporating petrological variation, intrusion of melt over a range of widths and a variable distribution of crystallization with depth have been developed in order to reconcile geophysical observations of the melt distribution at mid-ocean ridges with petrological and geological observations from the Oman ophiolite. Petrological variation has a first order control on the predicted distribution of melt within the crust and since geophysical observations are particularly sensitive to this distribution, petrological variation must be taken account of when the results of thermal models are compared with those of geophysical surveys. Petrological observations from ophiolites and geophysical observations from ridges can be related through thermal models that include petrological variation. In models where the large-

scale ophiolite compositional structure is reproduced a shallow melt lens with a near-solid floor can be generated. This feature is reproduced because the solidus temperature of the upper layer is lower than that of the lower layer. Letting intrusion occur throughout a region of nonzero width allows a high temperature zone several kilometers wide to be developed in the lower crust under the ridge axis. Steep isotherms may then be generated in the flanks of this region by hydrothermal cooling.

[70] The model results show that many sills crustal accretion models, where all of the lower crust forms by crystallization at its final depth and no vertical advection of solid material takes place, can be consistent both with the petrological observations from Oman and with the large-scale distribution of melt at the EPR inferred from geophysical observations. In order for these models to successfully reproduce the geophysical observations approximately 80% of the total hydrothermal cooling must take place at the flanks of the axial intrusion region, and this hydrothermal heat loss must operate down to Moho depths.

[71] Gabbro glacier models of crustal accretion, where all of the lower crust is formed by crystallization in a shallow melt lens before it is advected downward to its final depth, can also be consistent with the broad-scale geophysical and petrological observations. In this case, less than 50% of the hydrothermal heat loss occurs at the flanks of the axial region, and only modest amounts of heat need to be removed from Moho levels.

[72] While both many sills and gabbro glacier models can reproduce the large-scale geophysical and petrological observations, a hybrid model of crustal accretion is preferred where the uppermost part of the lower crust forms in the shallow melt lens and the lowermost crust forms by crystallization in situ. This distribution of crystallization allows detailed geophysical observations to be reproduced, such as the limited vertical extent of the shallow melt lens and its boundaries and the presence of melt bodies at

Moho depths. However, these features can be reproduced by a wide range of hybrid models, certainly including models where between 25% and 75% of the lower crust forms in the shallow melt lens. More detailed observations, both of the melt distribution at active ridges, and the petrological structure of ophiolites will be required in order to differentiate between gabbro glacier and many sills dominated models.

## Appendix A: Distribution of Hydrothermal Heat Removal in the Off-Axis Region

[73] Similarly to *Henstock et al.* [1993], the vertically integrated rate of heat removal,  $\hat{H}(x)$ , decays exponentially away from the edge of the axial region as

$$\hat{H}(x) \equiv \int_0^{z_c} H(x, \zeta) d\zeta = \begin{cases} 0 & A \leq x < A + \Delta, \\ H_{\max} \exp\left(\frac{A + \Delta - x}{\lambda}\right) & x \geq A + \Delta, \end{cases} \quad (\text{A1})$$

where  $H_{\max}$  is the maximum rate of heat removal,  $\Delta$  is a small distance (typically 100 m) introduced to control the temperature range over which heat is removed, and  $\lambda$  is a scaling length. The strength of hydrothermal circulation is chosen to vary with depth in an ad hoc way by first calculating a solution for the temperature structure and melt fraction in the axial region with no off-axis hydrothermal circulation present, and then setting

$$H(x, z) = \hat{H}(x) \left[ \chi(z) / \int_0^{z_c} \chi(\zeta) d\zeta \right], \quad (\text{A2})$$

where

$$\chi(z) = \begin{cases} [T - (T_i - 200)]c_p + (1 - \tau) & T > T_i - 200, \\ 0 & T \leq T_i - 200. \end{cases} \quad (\text{A3})$$

The hydrothermal circulation is strongest at depths where melt is present because  $\tau$  is the

equilibrium predicted melt fraction at a given depth in the axial region.

## Appendix B: Details of Thermal Balance in Axial Region

[74] The rate of heat flow into a volume element of the axial region of (infinitesimal) thickness  $dz$  due to vertical advection of fluid is given by the expression

$$\begin{aligned}
 & -d[\mathcal{F}_l(z)\rho(c_p T_i(z) + L_h)] \\
 & = -\left[\rho \frac{d\mathcal{F}_l}{dz}(c_p T_i + L_h) + \rho \mathcal{F}_l c_p \frac{dT_i}{dz}\right] dz. \quad (\text{B1})
 \end{aligned}$$

This expression accounts not only for the specific heat carried by the melt, but also the latent heat released by the melt which crystallizes within the volume element. Here  $T_i(z)$  is the injection temperature of the melt. The rate of heat flow into the volume element due to vertical advection (again taking into account possible latent heat release if the downgoing material is not completely crystallized) is given by the expression

$$\begin{aligned}
 & -d\{\mathcal{F}_s(z)\rho[c_p T(z) + (1 - \gamma(T(z))L_h]\} \\
 & = -\left[\rho \frac{d\mathcal{F}_s}{dz}(c_p T + (1 - \gamma)L_h) + \rho \mathcal{F}_s \left(c_p \frac{dT}{dz} - \frac{d\gamma}{dz} L_h\right)\right] dz. \quad (\text{B2})
 \end{aligned}$$

The horizontal motion of the extruded crust also produces advective heat transfer, and gives a rate of heat flow into the volume element of

$$-U\rho[c_p T + (1 - \tau)L_h] dz. \quad (\text{B3})$$

The expression for the rate of heat flow into the volume element due to vertical conduction of heat through the axial region is given by

$$-d\left[-Ak \frac{dT}{dz}\right] = Ak \frac{d^2 T}{dz^2} dz, \quad (\text{B4})$$

while horizontal temperature gradients in the off-axis region mean that heat is also conducted horizontally with a rate of heat flow into the volume element of

$$k \frac{\partial T}{\partial x} \Big|_A dz. \quad (\text{B5})$$

The partial derivative in this expression is calculated using the off-axis temperature solution.

[75] Within the axial lower crust, where no hydrothermal heat removal is permitted, the sum of expressions (B1)–(B5) is zero, giving the differential equation

$$\begin{aligned}
 & Ak \frac{d^2 T}{dz^2} - \rho \mathcal{F}_s c_p \frac{dT}{dz} - \rho \frac{d\mathcal{F}_s}{dz} c_p T - U\rho c_p T \\
 & = \frac{d}{dz}(\rho c_p \mathcal{F}_l T_i) - \frac{d}{dz}(\rho L_h \mathcal{F}_s \gamma) - U\rho \tau L_h - k \frac{\partial T}{\partial x} \Big|_A. \quad (\text{B6})
 \end{aligned}$$

[76] Substitution of the mass balance relationships (1) in (B6) gives (5). If hydrothermal circulation acts to cool the crust then an extra contribution of is added to the heat balance, producing a term  $+AH$  on the right hand side of (6).

## Appendix C: Method of Solution for Axial Thermal Structure

[77] Equations (5), (6) and (7) are used to determine the axial temperature structure for  $0 < z < z_g$ . Once the style and distribution of crystallization have been defined along with the crystallization behavior of the mantle melt,  $T_i(z)$ ,  $\theta(z)$ ,  $\gamma(T)$  and  $\tau(T, z)$  become known functions. Assuming that we also have an estimate for the horizontal conductive flux  $k\partial T/\partial x$  at  $x = A$ , these equations define a second order boundary value problem for  $T(z)$ . The boundary conditions that must be satisfied are

$$T(0) = 0, \quad (\text{C1})$$

$$T(z_g) = T_i(z_g), \quad (\text{C2})$$

$$\int_0^{z_g} H(z) dz = \hat{H}, \quad (\text{C3})$$

Boundary condition (C3) expresses the fact that the total depth integrated rate of heat removal by hydrothermal circulation is constrained to be  $\hat{H}$ .

[78] Within the axial region, we choose to define the hydrothermal circulation as function of temperature. We therefore introduce a parameter  $\alpha$  (which acts as an eigenvalue) such that

$$H(z) = \alpha \tilde{H}(T(z)) \quad (\text{C4})$$

where

$$\tilde{H}(T) = \begin{cases} \cos^2\left(\frac{\pi(T-450)}{300}\right) & 300 < T < 600 \\ 0 & \text{Otherwise} \end{cases} \quad (\text{C5})$$

The functional form of  $\tilde{H}(T)$  is such that hydrothermal circulation acts at temperatures between 300°C and 600°C, with peak effect at 450°C. The parameter  $\alpha$  acts as a scaling factor to ensure that boundary condition (C3) is satisfied, and must be solved for at the same time as we solve for the temperature structure.

[79] To solve the differential equation we define a constant  $W$  as

$$W = -\rho c_p \mathcal{F}_l(z_m) T_i(z_m) - \rho c_p U z_m T_i^0, \quad (\text{C6})$$

and introduce variables  $y_1, y_2, y_3$  and  $y_4$ , defined by

$$y_1 = T, \quad (\text{C7})$$

$$y_2 = \begin{cases} Ak \frac{dT}{dz} & z < z_m, \\ Ak \frac{dT}{dz} + \rho \mathcal{F}_s [L_h \gamma - c_p T] + W & z_m < z < z_c, \\ Ak \frac{dT}{dz} + W & z > z_c, \end{cases} \quad (\text{C8})$$

$$y_3 = \begin{cases} \int_0^z \alpha \tilde{H}(T(\zeta)) d\zeta & 0 < z < z_m, \\ \int_0^{z_m} \alpha \tilde{H}(T(\zeta)) d\zeta & z_m < z < z_g, \end{cases} \quad (\text{C9})$$

$$y_4 = \alpha. \quad (\text{C10})$$

The apparent jump in  $y_2$  of  $\rho \mathcal{F}_s(z_m)[L_h \gamma(T(z_m)) - c_p T(z_m)] + W$  at  $z = z_m$  is exactly balanced by the step change in  $AkdT/dz$  required by the delta function source (8). Thus  $y_2$  is continuous at  $z = z_m$  and, furthermore, is continuous at  $z = z_c$  since  $\mathcal{F}_s(z_c) = 0$ . It is clear from their definitions that the variables  $y_1, y_3$  and  $y_4$  are continuous everywhere, and so all the variables defined by equations (C7)–(C10) are continuous with depth. The boundary conditions (C1)–(C3) become

$$y_1(0) = 0, \quad y_1(z_g) = T_i(z_g), \quad (\text{C11})$$

$$y_3(0) = 0, \quad y_3(z_g) = \hat{H}. \quad (\text{C12})$$

[80] Differential equations for the variables  $y_1, y_2, y_3$  and  $y_4$  can be obtained by differentiating definitions (C7)–(C10) and using equations (5), (6) and (7). Thus in the upper crust, for  $z < z_m$ , we have

$$\frac{dy_1}{dz} = \frac{1}{Ak} y_2, \quad (\text{C13})$$

$$\frac{dy_2}{dz} = Ak \frac{d^2 T}{dz^2} \quad (\text{C14})$$

$$= \rho c_p U T - \rho c_p U T_i^0 - \rho L_h U \tau(T, z) - k \left. \frac{\partial T}{\partial x} \right|_A + A \alpha \tilde{H}(T) \quad (\text{C15})$$

$$= \rho c_p U y_1 - \rho c_p U T_i^0 - \rho L_h U \tau(y_1, z) - k \left. \frac{\partial T}{\partial x} \right|_A + A y_4 \tilde{H}(y_1), \quad (\text{C16})$$

$$\frac{dy_3}{dz} = y_4 \tilde{H}(y_1), \quad (\text{C17})$$

$$\frac{dy_4}{dz} = 0. \quad (\text{C18})$$

Similarly, in the lower crust, for  $z_m < z < z_c$ , we have

$$\frac{dy_1}{dz} = \frac{1}{Ak} [y_2 - \mathcal{F}_s(z)(\rho L_h \gamma(y_1) - \rho c_p y_1) - W], \quad (\text{C19})$$

$$\frac{dy_2}{dz} = Ak \frac{d^2 T}{dz^2} + \rho \frac{d\mathcal{F}_s}{dz} (L_h \gamma - c_p T) + \rho \mathcal{F}_s \frac{dT}{dz} \left( L_h \frac{d\gamma}{dT} - c_p \right) \quad (\text{C20})$$

$$\begin{aligned} &= \rho c_p \mathcal{F}_s \frac{dT}{dz} + \rho c_p U (1 - \theta) T + \rho c_p \mathcal{F}_l \frac{dT_i}{dz} - \rho c_p U (1 - \theta) T_i \\ &\quad - \rho L_h \mathcal{F}_s \frac{dT}{dz} \frac{d\gamma}{dT} - \rho L_h U \sigma (1 - \theta) - k \left. \frac{\partial T}{\partial x} \right|_A \\ &\quad - \rho L_h U \theta \gamma + \rho c_p U \theta T + \rho L_h \mathcal{F}_s \frac{dT}{dz} \frac{d\gamma}{dT} - \rho c_p \mathcal{F}_s \frac{dT}{dz} \end{aligned} \quad (\text{C21})$$

$$\begin{aligned} &= \rho c_p U T + \rho c_p \mathcal{F}_l \frac{dT_i}{dz} - \rho c_p U (1 - \theta) T_i \\ &\quad - \rho L_h U (\sigma (1 - \theta) + \gamma \theta) - k \left. \frac{\partial T}{\partial x} \right|_A \end{aligned} \quad (\text{C22})$$

$$\begin{aligned}
 &= \rho c_p U y_1 + \rho c_p \mathcal{F}_l(z) \frac{dT_i}{dz} - \rho c_p U (1 - \theta(z)) T_i(z) \\
 &\quad - \rho L_h U \tau(y_1, z) - k \left. \frac{\partial T}{\partial x} \right|_A, \quad (C23)
 \end{aligned}$$

$$\frac{dy_3}{dz} = 0, \quad (C24)$$

$$\frac{dy_4}{dz} = 0. \quad (C25)$$

Finally, in the mantle, for  $z_c < z < z_g$ , we have

$$\frac{dy_1}{dz} = \frac{1}{Ak} (y_2 - W), \quad (C26)$$

$$\frac{dy_2}{dz} = Ak \frac{d^2 T}{dz^2} \quad (C27)$$

$$= \rho c_p U T - \rho c_p U T_i - \rho L_h U (1 - \tau) - k \left. \frac{\partial T}{\partial x} \right|_A \quad (C28)$$

$$= \rho c_p U y_1 - \rho c_p U T_i(z) - \rho L_h U (1 - \tau(y_1, z)) - k \left. \frac{\partial T}{\partial x} \right|_A, \quad (C29)$$

$$\frac{dy_3}{dz} = 0, \quad (C30)$$

$$\frac{dy_4}{dz} = 0. \quad (C31)$$

The differential equations have therefore been written entirely in terms of known functions of  $y_1, y_2, y_3, y_4$  and  $z$ . Together with the boundary conditions, these differential equations constitute a standard two point boundary value problem. The desired complementary functions show exponential decay, and so the equations are solved numerically using a relaxation method [Press *et al.*, 1992].

## Appendix D: Fourier Sine Series Solution for Off-Axis Temperature Structure

[81] The equation to be solved at each stage of the iteration is

$$U \frac{\partial T}{\partial x} - \kappa \left( \frac{\partial^2 T}{\partial x^2} + \frac{\partial^2 T}{\partial z^2} \right) = \hat{Q}(x, z), \quad (D1)$$

for  $x \geq A$ ,  $0 \leq z \leq z_l$ , subject to the boundary conditions  $T(A, z) = T_A(z)$ ,  $T(x, 0) = 0$ ,  $T(x, z_l) = T_l$  and  $T \rightarrow T_l z / z_l$  as  $x \rightarrow \infty$ , where  $T_A(z)$  is the one-dimensional temperature solution in the axial region and  $T_l = T_A(z_l)$ . The solution is calculated as the sum of two parts:  $T_0$ , the solution of the homogeneous problem satisfying the given (inhomogeneous) boundary conditions, and  $T_1$ , the solution of the inhomogeneous problem which vanishes on all boundaries.

[82] The solution to the homogeneous problem is written as

$$T_0(x, z) = \frac{T_l z}{z_l} + \sum_{m=1}^{\infty} f_m(x) \sin\left(\frac{m\pi z}{z_l}\right), \quad (D2)$$

which automatically satisfies the boundary conditions at  $z = 0$  and  $z = z_l$ . Substitution into the governing equation shows that the  $f_m$  satisfy

$$\frac{d^2 f_m}{dx^2} - \frac{U}{\kappa} \frac{df_m}{dx} - \frac{m^2 \pi^2}{z_l^2} f_m = 0 \quad (D3)$$

and so

$$f_m(x) = A_m e^{a_m(x-A)} + B_m e^{b_m(x-A)}, \quad (D4)$$

where

$$a_m = \frac{U}{2\kappa} \left( 1 - \sqrt{1 + \frac{4m^2 \pi^2 \kappa^2}{U^2 z_l^2}} \right), \quad (D5)$$

$$b_m = \frac{U}{2\kappa} \left( 1 + \sqrt{1 + \frac{4m^2 \pi^2 \kappa^2}{U^2 z_l^2}} \right). \quad (D6)$$

Since  $T$  decays as  $x \rightarrow \infty$ , we reject the exponentially growing solution by setting  $B_m = 0$ . The boundary condition at  $x = A$  gives

$$T_A(z) = \frac{T_l z}{z_l} + \sum_{m=1}^{\infty} A_m \sin\left(\frac{m\pi z}{z_l}\right), \quad (D7)$$

and so

$$A_m = \frac{2}{z_l} \int_0^{z_l} \left( T_A(z) - \frac{T_l z}{z_l} \right) \sin\left(\frac{m\pi z}{z_l}\right) dz \quad (\text{D8})$$

$$= (-1)^m \frac{2T_l}{m\pi} + \frac{2}{z_l} \int_0^{z_l} T_A(z) \sin\left(\frac{m\pi z}{z_l}\right) dz. \quad (\text{D9})$$

[83] To solve the inhomogeneous equation we follow *Morton and Sleep* [1985] in parameterizing the continuous heat source field  $\hat{Q}(x, z)$  as a discrete sum of point sources:

$$\hat{Q}(x, z) = \sum_{ij} \hat{Q}_{ij} \delta(x - x_i) \delta(z - z_j). \quad (\text{D10})$$

Since the boundary conditions are homogeneous we can calculate the total solution by superposition of the solution for each term in the sum. Representing the solution for the delta function at  $(x_i, z_j)$  as

$$T_1^{ij}(x, z) = \sum_{m=1}^{\infty} g_m(x) \sin\left(\frac{m\pi z}{z_l}\right), \quad (\text{D11})$$

which again satisfies by construction the boundary conditions at  $z = 0$  and  $z = z_l$ , we find that

$$\frac{d^2 g_m}{dx^2} - \frac{U}{\kappa} \frac{dg_m}{dx} - \frac{m^2 \pi^2}{z_l^2} g_m = -\frac{2\hat{Q}_{ij}}{\kappa z_l} \sin\left(\frac{m\pi z_j}{z_l}\right) \delta(x - x_i). \quad (\text{D12})$$

The solution to this equation which satisfies  $g_m(A) = 0$  and  $g_m(x) \rightarrow 0$  as  $x \rightarrow \infty$  is

$$g_m(x) = \begin{cases} \frac{2\hat{Q}_{ij}}{\kappa z_l (b_m - a_m)} \sin\left(\frac{m\pi z_j}{z_l}\right) \left[ e^{b_m(x-A)} - e^{a_m(x-A)} \right] e^{-b_m(x_i-A)} & x < x_i, \\ \frac{2\hat{Q}_{ij}}{\kappa z_l (b_m - a_m)} \sin\left(\frac{m\pi z_j}{z_l}\right) \left[ e^{-a_m(x_i-A)} - e^{-b_m(x_i-A)} \right] e^{a_m(x-A)} & x > x_i. \end{cases} \quad (\text{D13})$$

This expression is in a suitable form for numerical calculation, and the Fourier series sums (D2) and (D11) can be efficiently carried out using an FFT implementation of the discrete sine transform [*Press et al.*, 1992].

## Acknowledgments

[84] The authors would like to thank Mathilde Cannat for an informal review, Chris MacLeod for providing data and Mike Bickle, Joe Cann, Mathilde Cannat, Laurence Coogan, Wayne Crawford, Javier Escartin, Tim Jupp, Chris MacLeod,

Catherine Mével, Adolphe Nicolas and Will Wilcock for discussions and suggestions. Norm Sleep and Jun Korenaga are thanked for their formal reviews which helped to improve the quality of this manuscript. This work was supported by an EU Marie Curie Individual Fellowship to JM and an Entente Cordiale Scholarship to TH.

## References

- Asimow, P. D. (2002), Steady-state Mantle-Melt Interactions in One Dimension: 2. Thermal Interactions and Irreversible Terms, *J. Petrol.*, *43*, 1707–1724.
- Asimow, P. D., and M. S. Ghiorso (1998), Algorithmic modifications extending MELTS to calculate subsolidus phase relations, *Am. Mineral.*, *83*, 1127–1131.
- Babcock, J. M., A. J. Harding, G. M. Kent, and J. A. Orcutt (1998), An examination of along-axis variation of magma chamber width and crustal structure on the East Pacific Rise between 13°30'N and 12°20'N, *J. Geophys. Res.*, *103*, 30,451–30,467.
- Baker, E. T., Y. J. Chen, and J. Phipps Morgan (1996), The relationship between near-axis hydrothermal cooling and the spreading rate of mid-ocean ridges, *Earth Planet. Sci. Lett.*, *142*, 137–145.
- Boudier, F., A. Nicolas, and B. Ildefonse (1996), Magma chambers in the Oman ophiolite: Fed from the top and the bottom, *Earth Planet. Sci. Lett.*, *144*, 239–250.
- Browning, P. (1984), Cryptic variation within the cumulate sequence of the Oman ophiolite: Magma chamber depth and petrological implications, in *Ophiolites and Oceanic Lithosphere*, *Geol. Soc. London Spec. Publ.*, *13*, 71–82.
- Cann, J. R. (1974), A model for ocean crust structure developed, *Geophys. J. R. Astron. Soc.*, *39*, 169–187.
- Carbotte, S. M., A. Solomon, and G. Ponce-Correa (2000), Evaluation of morphological indicators of magma supply and segmentation from a seismic reflection study of the East Pacific Rise 15°30'–17°N, *J. Geophys. Res.*, *105*, 2737–2759.
- Chen, Y. J. (2001), Thermal effects of gabbro accretion from a deeper second melt lens at the fast spreading East Pacific Rise, *J. Geophys. Res.*, *106*, 8581–8588.
- Chenevez, J., and A. Nicolas (1997), Crustal feeding in the Oman ophiolite: From the top and from the bottom?: A thermal and mass balance model, *Geophys. Res. Lett.*, *24*, 1811–1814.
- Chenevez, J., P. Machetel, and A. Nicolas (1998), Numerical models of magma chambers in the Oman ophiolite, *J. Geophys. Res.*, *103*, 15,443–15,455.
- Cherkaoui, A. S. M., W. S. D. Wilcock, R. A. Dunn, and D. R. Toomey (2003), A numerical model of hydrothermal cooling and crustal accretion at a fast spreading mid-ocean ridge, *Geochem. Geophys. Geosyst.*, *4*(9), 8616, doi:10.1029/2001GC000215.
- Cochran, J. R., and W. R. Buck (2001), Near-axis subsidence rates, hydrothermal circulation, and thermal structure of mid-ocean ridge crests, *J. Geophys. Res.*, *106*, 19,233–19,258.
- Collier, J. S., and S. C. Singh (1997), Detailed structure of the top of the melt body beneath the East Pacific Rise at 9°40'N

- from waveform inversion of seismic reflection data, *J. Geophys. Res.*, *102*, 20,287–20,304.
- Coogan, L. A., G. R. T. Jenkin, and R. N. Wilson (2002a), Constraining the cooling rate of the lower oceanic crust: A new approach applied to the Oman ophiolite, *Earth Planet. Sci. Lett.*, *1999*, 127–146.
- Coogan, L. A., K. M. Gillis, C. J. MacLeod, G. M. Thompson, and R. Hkinian (2002b), Petrology and geochemistry of the lower ocean crust formed at the East Pacific Rise and exposed at Hess Deep: A synthesis and new results, *Geochem. Geophys. Geosyst.*, *3*(11), 8604, doi:10.1029/2001GC000230.
- Coogan, L. A., G. M. Thompson, and C. J. MacLeod (2002c), A textural and geochemical investigation of high level gabbros from the Oman ophiolite: Implications for the role of the axial magma chamber at fast spreading ridges, *Lithos*, *63*, 67–82.
- Coogan, L. A., N. C. Mitchell, and M. J. O'Hara (2003), Roof assimilation at fast spreading ridges: An investigation combining geophysical, geochemical, and field evidence, *J. Geophys. Res.*, *108*(B1), 2002, doi:10.1029/2001JB001171.
- Crawford, W. C., and S. C. Webb (2002), Variations in the distribution of magma in the lower crust and at the Moho beneath the East Pacific Rise at 9°–10°N, *Earth Planet. Sci. Lett.*, *203*, 117–130.
- Detrick, R. S., P. Buhl, E. Vera, J. Mutter, J. Orcutt, J. Madsen, and T. Brocher (1987), Multi-channel seismic imaging of a crustal magma chamber along the East Pacific Rise, *Nature*, *326*, 35–41.
- Dewey, J. F., and W. S. F. Kidd (1977), Geometry of plate accretion, *Geol. Soc. Am. Bull.*, *88*, 960–968.
- Dunn, R. A., D. R. Toomey, and S. C. Solomon (2000), Three-dimensional seismic structure and physical properties of the crust and shallow mantle beneath the East Pacific Rise at 9°30'N, *J. Geophys. Res.*, *105*, 23,537–23,555.
- Garmany, J. (1989), Accumulations of melt at the base of young oceanic crust, *Nature*, *340*, 620–630.
- Garrido, C. J., P. B. Kelemen, and G. Hirth (2001), Variation of cooling rate with depth in lower crust formed at an oceanic spreading ridge plagioclase crystal size distributions in gabbros from the Oman ophiolite, *Geochem. Geophys. Geosyst.*, *2*, Paper number 2000GC000136.
- Ghiorso, M. S., and R. O. Sack (1995), Chemical mass transfer in magmatic processes: IV. A revised and internally consistent thermodynamic model for the interpolation and extrapolation of liquid-solid equilibria in magmatic systems at elevated temperatures and pressures, *Contrib. Mineral. Petrol.*, *119*, 197–212.
- Gillis, K. M. (1995), Controls of hydrothermal alteration in a section of fast-spreading oceanic crust, *Earth Planet. Sci. Lett.*, *134*, 473–489.
- Hale, L. D., C. J. Morton, and N. H. Sleep (1982), Reinterpretation of seismic reflection data over the East Pacific Rise, *J. Geophys. Res.*, *87*, 7707–7717.
- Harding, A. J., J. A. Orcutt, M. E. Kappus, E. E. Vera, J. C. Mutter, P. Buhl, R. S. Detrick, and T. M. Brocher (1989), Structure of young oceanic crust at 13°N on the East Pacific Rise from expanding spread profiles, *J. Geophys. Res.*, *94*, 12,163–12,196.
- Hekinian, R., D. Bideau, J. Francheteau, J. L. Cheminee, R. Armijo, P. Lonsdale, and N. Blum (1993), Petrology of the East Pacific Rise crust and upper mantle exposed in Hess Deep (Eastern Equatorial Pacific), *J. Geophys. Res.*, *98*, 8069–8094.
- Henstock, T. J., A. W. Woods, and R. S. White (1993), The accretion of oceanic crust by episodic sill intrusion, *J. Geophys. Res.*, *98*, 4143–4161.
- Herron, T. J., P. L. Stoff, and P. Buhl (1980), Magma chambers and mantle reflections—East Pacific Rise, *Geophys. Res. Lett.*, *7*, 989–992.
- Hooft, E. E. E., R. S. Detrick, and G. M. Kent (1997), Seismic structure and indicators of magma budget along the southern East Pacific Rise, *J. Geophys. Res.*, *102*, 27,319–27,340.
- Jupp, T., and A. Schultz (2000), A thermodynamic explanation for black smoker temperatures, *Nature*, *403*, 880–883.
- Kelemen, P. B., G. Hirth, N. Shimizu, M. Spiegelman, and H. J. B. Dick (1997a), A review of melt migration processes in the adiabatically upwelling mantle beneath oceanic spreading ridges, *Philos. Trans. R. Soc. London*, *A355*, 283–318.
- Kelemen, P. B., K. Koga, and N. Shimizu (1997b), Geochemistry of gabbro sills in the crust-mantle transition zone of the Oman ophiolite: Implications for the origin of the oceanic lower crust, *Earth Planet. Sci. Lett.*, *146*, 475–488.
- Kent, G. M., A. J. Harding, and J. A. Orcutt (1993a), Distribution of magma beneath the East Pacific Rise between the clipperton transform and the 9°17'N deval from forward modeling of common depth point data, *J. Geophys. Res.*, *98*, 13,945–13,969.
- Kent, G. M., A. J. Harding, and J. A. Orcutt (1993b), Distribution of magma beneath the East Pacific Rise near the 9°03'N overlapping spreading center from forward modeling of common depth point data, *J. Geophys. Res.*, *98*, 13,971–13,995.
- Kinzler, R. J., and T. L. Grove (1992), Primary magmas of midocean ridge basalts: 2. Applications, *J. Geophys. Res.*, *97*, 6907–6926.
- Koga, K. T., P. B. Kelemen, and N. Shimizu (2001), Petrogenesis of the crust-mantle transition zone and the origin of lower crustal wehrlite in the Oman ophiolite, *Geochem. Geophys. Geosyst.*, *2*, doi:10.1029/2000GC000132.
- Korenaga, J., and P. B. Kelemen (1997), Origin of gabbro sills in the Moho transition zone of the Oman ophiolite: Implications for magma transport in the oceanic lower crust, *J. Geophys. Res.*, *102*, 27,729–27,749.
- Korenaga, J., and P. B. Kelemen (1998), Melt migration through the oceanic lower crust; a constraint from melt percolation modeling with finite solid diffusion, *Earth Planet. Sci. Lett.*, *156*, 1–11.
- Lister, C. R. B. (1995), Heat transfer between magmas and hydrothermal systems, or, 6 lemmas in search of a theorem, *Geophys. J. Int.*, *120*, 45–59.
- MacLennan, J., M. Jull, D. McKenzie, L. Slater, and K. Gronvöld (2002), The link between volcanism and deglaciation in Iceland, *Geochem. Geophys. Geosyst.*, *3*(11), 1062, doi:10.1029/2001GC000282.

- MacLeod, C. J., and G. Yaouancq (2000), A fossil melt lens in the Oman ophiolite: Implications for magma chamber processes at fast spreading ridges, *Earth Planet. Sci. Lett.*, *176*, 357–373.
- Mainprice, D. (1997), Modelling the anisotropic seismic properties of partially molten rocks found at mid-ocean ridges, *Tectonophysics*, *279*, 161–179.
- Manning, C. E., P. E. Weston, and K. I. Mahon (1996), Rapid high-temperature metamorphism of East Pacific rise gabbros from Hess deep, *Earth Planet. Sci. Lett.*, *144*, 123–132.
- McKenzie, D., and M. J. Bickle (1988), The volume and composition of melt generated by extension of the lithosphere, *J. Petrol.*, *29*, 625–679.
- Morton, J. L., and N. H. Sleep (1985), A Mid-Ocean Ridge Thermal Model: Constraints on the Volume of Axial Hydrothermal Heat Flux, *J. Geophys. Res.*, *90*, 1345–1353.
- Nicolas, A. (1989), *Structure of Ophiolites and Dynamics of Oceanic Lithosphere*, Kluwer Acad., Norwell, Mass.
- Nicolas, A., and F. Boudier (1995), Mapping oceanic ridge segments in Oman ophiolites, *J. Geophys. Res.*, *100*, 6179–6197.
- Nicolas, A., D. Mainprice, and F. Boudier (2003), High temperature seawater circulation throughout crust of oceanic ridges—a model derived from the Oman ophiolites, *Geophys. Res. Abstracts*, *5*, 09476.
- Pallister, J., and C. Hopson (1981), Semail ophiolite suite: Field relations, phase variation, cryptic variation and layering, and a model of a spreading ridge magma chamber, *J. Geophys. Res.*, *86*, 2593–2644.
- Phipps Morgan, J., and Y. Chen (1993), The genesis of oceanic crust, magma injection, hydrothermal circulation and crustal flow, *J. Geophys. Res.*, *98*, 6283–6297.
- Ponce-Correa, G. J., J. C. Mutter, and S. Carbotte (1999), Fresnel zone: A pitfall in seismic imaging of mid-ocean ridge magma lenses, *Geophys. Res. Lett.*, *26*, 3021–3024.
- Press, W. H., S. A. Teukolsky, W. T. Vetterling, and B. P. Flannery (1992), *Numerical recipes in Fortran 77*, 2nd ed., Cambridge Univ. Press, New York.
- Quick, J. E., and R. P. Denlinger (1993), Ductile deformation and the origin of layered gabbro in ophiolites, *J. Geophys. Res.*, *98*, 14,015–14,027.
- Shah, A. K., and W. R. Buck (2001), Causes for axial high topography at mid-ocean ridges and the role of crustal thermal structure, *J. Geophys. Res.*, *106*, 30,865–30,879.
- Shah, A. K., and W. R. Buck (2003), Plate bending stresses at axial highs, and implications for faulting behaviour, *Earth Planet. Sci. Lett.*, *211*, 343–356.
- Singh, S. C., G. M. Kent, J. S. Collier, A. J. Harding, and J. A. Orcutt (1998), Melt to mush variations in crustal magma properties along the ridge crest at the southern East Pacific Rise, *Nature*, *394*, 874–878.
- Singh, S. C., J. S. Collier, A. J. Harding, G. M. Kent, and J. A. Orcutt (1999), Seismic evidence for a hydrothermal layer above the solid roof of the axial magma chamber at the southern East Pacific Rise, *Geology*, *27*, 219–222.
- Sinton, J. M., and R. S. Detrick (1992), Mid-ocean ridge magma chambers, *J. Geophys. Res.*, *97*, 197–216.
- Sleep, N. H. (1975), Formation of oceanic crust: Some thermal constraints, *J. Geophys. Res.*, *80*, 4037–4042.
- Sleep, N. H. (1991), Hydrothermal circulation, Anhydrite Precipitation, and Thermal Structure at Ridge Axes, *J. Geophys. Res.*, *96*, 2375–2387.
- Teagle, D. A. H., M. J. Bickle, and J. C. Alt (2003), Recharge flux to ocean-ridge black smoker systems: A geochemical estimate from ODP Hole 504B, *Earth Planet. Sci. Lett.*, *210*, 81–89.
- Vera, E. E., J. C. Mutter, P. Buhl, J. A. Orcutt, A. J. Harding, M. E. Kappus, R. S. Detrick, and T. M. Brocher (1990), The structure of 0- to 0.2-m. y.-old oceanic crust at 9°N on the East Pacific Rise from expanded spread profiles, *J. Geophys. Res.*, *95*, 15,529–15,556.
- Von Damm, K. L., J. M. Edmond, B. Grant, C. I. Measures, B. Walden, and R. F. Weiss (1985), Chemistry of submarine hydrothermal solutions at 21°N, East Pacific Rise, *Geochim. Cosmochim. Acta*, *49*, 2197–2220.